MULTI-SCALE MODELLING OF O2 AND O3-TYPE MATERIALS FOR UTILIZATION AS CORE-SHELL MATERIALS

By

MAKHUBELA PRECIOUS GUGU

DISSERTATION

Submitted in the fulfilment of the requirements for the degree of

MASTER OF SCIENCE

in

PHYSICS

in the

FACULTY OF SCIENCE AND AGRICULTURE
(School Of Physical and Mineral Sciences)

at the

UNIVERSITY OF LIMPOPO

SUPERVISOR: PROF. R.S. LEDWABA

CO-SUPERVISORS: PROF. P.E. NGOEPE

: DR. K.M. KGATWANE

2024

DECLARATION

I declare that the work submitted to the University of Limpopo, Turfloop Campus for the Master of Science degree in Physics titled MULTI-SCALE MODELLING OF O2 AND O3-TYPE MATERIALS FOR UTILIZATION AS CORE-SHELL MATERIALS, is my own work and that all the sources that I have used or quoted have been indicated and acknowledged by means of complete references and that this work has not been submitted before for any other degree at any other institution.

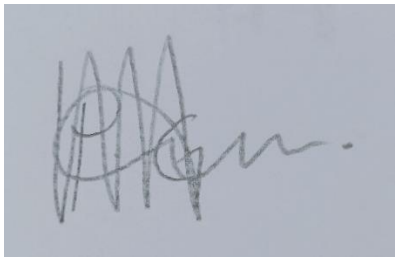

31/01/2024

…… ……..

Precious Gugu Makhubela **Date**

DEDICATION

This work is dedicated to

My late parents

Ester Nkuna

Joseph Makhubela

My supportive siblings

Hendry J Makhubela

Solomon S Makhubela

Lindiwe Makhubela

My son

Mayibongwe Mandlazi

ACKNOWLEDGEMENTS

I extend my gratitude to the University of Limpopo for granting me the opportunity to enrol in their Master of Science degree. I am sincerely thankful to my supervisor, Prof RS Ledwaba, for her immense patience, consultation, and guidance throughout the completion of this research. My journey would not have been possible without the valuable assistance of my co-supervisors, Prof PE Ngoepe and Dr KM Kgatwane, who generously shared their knowledge and skills. The support provided by the National Research Fund (NRF) and the Materials Modelling Centre (MMC) was instrumental in funding my study and facilitating the computational aspects of this work. Special recognition goes to the Centre for High-Performance Computing (CHPC) facility in South Africa, whose resources were crucial to the successful completion of this project. Lastly, I want to express my appreciation to my family, particularly my brothers and sister, whose unwavering belief in me has been a source of motivation and encouragement throughout this process.

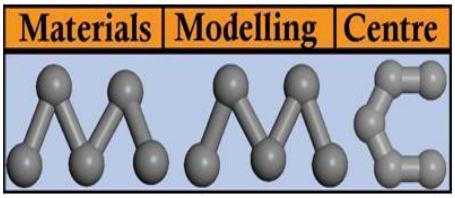

ABSTRACT

The automotive industry is currently prioritizing the development of lithium-ion batteries for electric vehicles due to the energy crisis and environmental concerns. These batteries rely on breakthroughs in cathode materials to achieve high-energy-density variants. However, the scarcity and cost of raw materials like cobalt and nickel underscore the need for affordable alternatives. Li_2MnO_3, made with abundant and economical manganese, offers higher capacity than traditional oxides but faces challenges like poor stability and low conductivity. Researchers are addressing these issues through methods such as elemental doping, surface modification, and a newly developed core-shell architecture to enhance electrochemical performance. The core-shell structure improves physical structure and conductivity and prevents undesirable reactions during charge and discharge processes.

While the core-shell architecture has been investigated in the context of Li_2MnO_3, this study aims to pioneer the use of Li_2MnO_3 as the core material. The research delves into the intricate process of modelling and developing core-shell systems intended to serve as electrode materials with coating interfaces. Before creating these systems, the study investigates the electrochemical performance of Li_2MnO_3 through the delithiation process of $Li_{2-x}MnO_3$ ($0 \leq x \leq 1$) to gain a better understanding of its electrochemical behaviour before coating. The research utilizes density functional theory to investigate the structural and electronic characteristics of both the bulk structure of Li_2MnO_3 and delithiated structures of $Li_{2-x}MnO_3$. Calculations reveal that the material has a monoclinic structure, with lithium contributing the least to the overall density of states. Electronic band structures indicate a shift in conductivity during the delithiation process, transitioning from semiconductive to magnetic metal behaviour.

Subsequently, two core-shell systems, consisting of 1434 and 435 atoms, were generated by coating O3-type Li_2MnO_3 with O2-type $Li_{0.69}MnO_2$, chosen for its high ionic conductivity and resistance to spinel transformation during cycling. Molecular dynamics simulations were conducted to optimize the conditions for these core-shell systems using the Nose-Hoover thermostat under NVT, NST, and NPT ensembles. The simulations involved varying parameters such as steps, timesteps, and temperature to investigate their effects on the core-shell systems. It is observed that

the larger system outperforms the smaller one. Disordered behaviour was noted after 150,000 steps and 0.0001 timesteps, and temperature variations resulted in disorder, with the system regaining its crystalline form at 1500 K for both NVT and NPT ensembles after initial disorder at 1200 K and 900 K, respectively.

Progress in this work has shown that the core-shell system is adequate for prevention of simultaneous oxygen and lithium loss during analysis of the structural snapshots when subjected to temperature

TABLE OF CONTENTS

LIST OF TABLES

LIST OF FIGURES

CHAPTER 1

INTRODUCTION AND BACKGROUND

1.1. Background

In recent years, there has been a noticeable surge in energy demand associated with substantial economic development. The global need for energy storage systems is on the rise due to their perceived practicality, environmental friendliness, and long-term safety [1, 2]. The combustion of fossil fuels not only pollutes the environment but also releases a significant amount of greenhouse gases [3, 4]. With many governments advocating for the shift towards an eco-friendly economy and committing to carbon-peak and carbon-neutrality goals by 2030 and 2060, expediting the energy transition becomes crucial by replacing fossil fuels with clean energy [5, 6]. Clean energy is defined as energy that avoids pollutant emissions, can be directly utilized in various applications, and rapidly regenerates and replenishes after consumption [5].

The main challenge faced by renewable energy systems is intermittent power generation, as sources like solar and wind are dependent on weather conditions [7]. Lithium-ion batteries play a vital role in addressing energy storage needs by allowing the collection and utilization of surplus energy generated during peak production times. This stored energy can be subsequently released during periods characterized by low renewable energy generation or high demand, ensuring a stable and dependable power source [8]. Lithium-ion batteries are prevalent in various contemporary applications due to their characteristics such as high voltage, substantial energy density, cost-effectiveness, lightweight construction, and rechargeable capabilities [9].

1.2. Lithium-ion batteries

Lithium-ion batteries (LIBs) hold significant prominence as a primary battery technology and find extensive use in personal electronic devices like smartphones, laptops, digital cameras, and health monitoring systems [10]. These batteries have emerged as the primary power source due to their consistent electrochemical performance, minimal environmental impact, and impressive charge retention capabilities. Nevertheless, there is still a need for lithium-ion batteries that are safer, longer-lasting, possess higher energy density, and come at a lower cost to meet the demands of large-scale applications like electric vehicles (EVs) and stationary electrical energy storage [11]. One approach to achieve enhanced energy density involves raising the charging voltage of cells equipped with positive electrodes based on NMC (Nickel, Manganese, Cobalt) [12].

Recently, significant attention has been directed towards layered transition metal oxides, capable of accommodating more than one lithium unit per molecule, as a key component in the progress of enhanced cathode materials [13]. The progress in developing cathode materials like Li-Mn-O-oxides is crucial for the lithium-ion battery industry, considering the cost implications of cobalt and nickel resources and the safety considerations associated with cathode materials based on cobalt and nickel [14]. The O3-type layered transition metal oxides have been a significant success among the different prospective cathode materials since they demonstrate competitive performance and a comparable energy density to lithium-ion batteries due to composite and structure optimization [14].

1.2.1. Operating lithium-ion batteries

Lithium-ion batteries comprise four distinct elements: the anode, responsible for electron flow through a wire; the cathode, influencing the capacity and voltage of a Li-ion battery; the electrolyte, facilitating the exclusive movement of ions; and the separator, serving as the complete barrier between the cathode and anode.

This holds true whether it's the miniature Li-Ion battery in your smartwatch or the massive Li-Ion batteries propelling electric vehicles. The metal lithium serves as the cathode, and the chemical reactions between lithium and the electrolyte are what make these batteries peculiar [15]. There is an ever-growing worldwide need for clean, sustainable, renewable, environmentally safe energy technologies as a replacement for traditional hydrocarbon fuels. Therefore, the development of this class of batteries is essential for the battery industry [16].

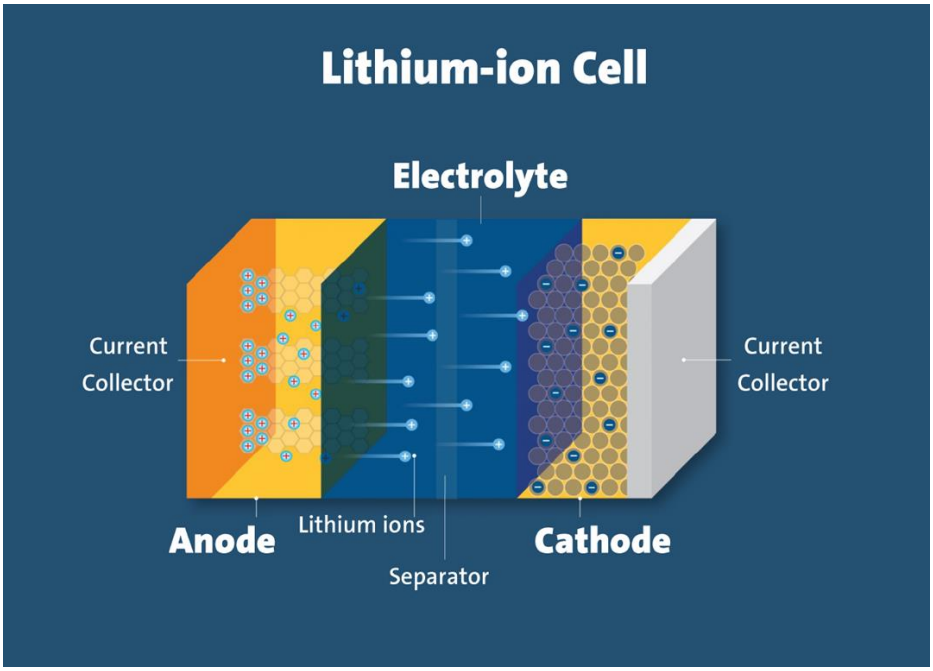

Figure 1.1. Illustration of what goes on inside a lithium-ion battery cell.

1.2.2. Common applications of lithium-ion batteries

Common applications include portable electronics such as smartphones, laptops, and tablets, where lithium-ion batteries provide long-lasting power in compact form factors. Furthermore, they play a crucial role in the electric vehicle (EV) and hybrid electric vehicle (HEV) sector by fueling the majority of electric cars, contributing significantly to the worldwide transition to sustainable transportation.

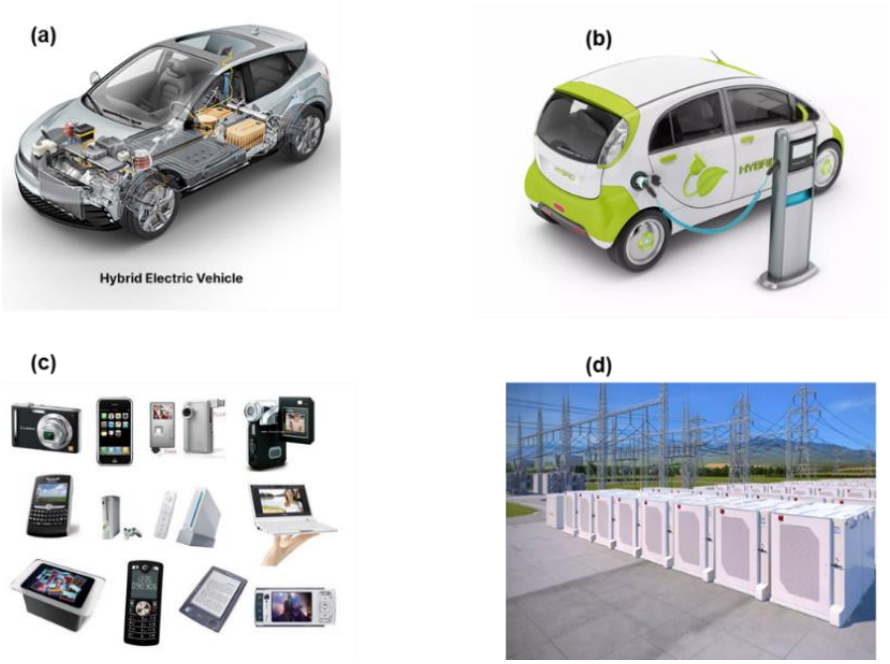

Figure 1.2. Examples of applications for lithium-ion batteries include (a) hybrid electric vehicles, (b) electric vehicles, (c) portable devices, and (d) storage facilities such as smart grids.

1.3. Literature review

1.3.1. Li_2MnO_3

The O3-type Li_2MnO_3, a layered metal oxide cathode material, holds promise for application in large-scale energy storage systems like electricity power grids and electric vehicles due to its demonstrated high specific capacity and energy density [17]. However, during charge and discharge, structural changes occur, leading to the transition metal migrating from the cathode material into the electrolyte [14]. This interaction with the electrolyte causes capacity degradation in the cathode, resulting in a shortened battery lifespan [14, 17, 18]. Despite its structural and electrochemical appeal, the Li_2MnO_3 with an O3-type structure was initially considered electrochemically inert for lithium insertion and extraction within the voltage range of 2.0 V to 4.4 V in its microcrystalline state. Nevertheless, it still boasts a theoretical capacity of 460 $mAhg^{-1}$ for lithium extraction [19]. Initially thought to be inert due to the presence of Mn^{4+} ions that

couldn't be oxidized to enable Li^+ ion extraction, recent research indicates that the electrochemical activity of this compound is attributed to oxygen removal, Li^+-H^+ ion exchange, and oxygen deficiency, introducing Mn^{3+} ions rather than Mn^{4+} oxidation, which is now recognized as the accepted electrochemical mechanism for this compound [20].

Klein et al. conducted research aimed at enhancing the cycling stability of Li_2MnO_3 through surface treatment. They achieved this by creating an electrochemically stable and cobalt-free cathode material, wherein Li_2MnO_3 was soaked in nickel nitrate and subsequently calcinated at 650ºC. According to their findings, the surface-modified samples demonstrated notable improvements in cycling stability and rate capability. Specifically, the material with nickel content exhibited a capacity of 173 $mAhg^{-1}$ at a rate of C/10, 104 $mAhg^{-1}$ at a rate of 3C, and maintained a consistent capacity of 155 $mAhg^{-1}$ at a rate of C/5 [21].

Chennakrishnan et al. utilized the sol-gel method to synthesize Li_2MnO_3 nanoparticles, and they disclosed that samples prepared through sol-gel with citric acid exhibited a maximum capacity of 27 $mAhg^{-1}$. The charge and discharge voltages applied during the process were 3 V and 4 V [22]. Additionally, Amalraj and his colleagues employed a self-combustion reaction to synthesize nano-sized Li_2MnO_3 particles. They observed that, in the case of nano-Li_2MnO_3, lithium extraction occurred at significantly lower potentials compared to micron-sized Li_2MnO_3. Their structural analysis of nano-Li_2MnO_3 revealed a partial transition from layered $LiMnO_2$ to a spinel-type ordering [19].

1.3.2. Structural properties of Li_2MnO_3

Li_2MnO_3 is a *C2/m* space group material with a cubic-closely packed (ABC) layered structure, with the transition-metal layer having an ordered atomic arrangement with Li atoms at the 2b site and Mn atoms at the 4g site [23].

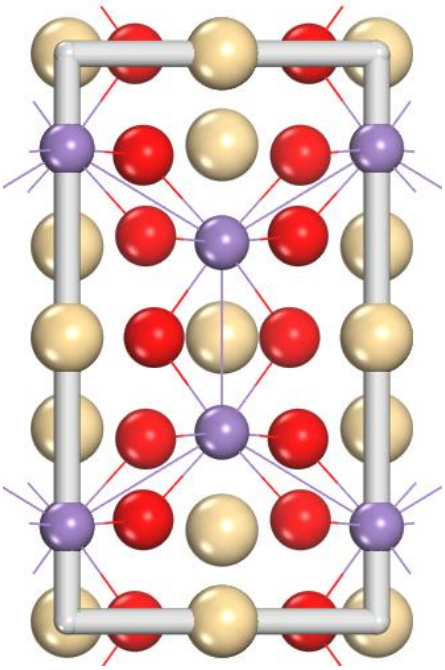

Figure 1.3. The monoclinic crystal structure of Li_2MnO_3.

1.3.3. Structural properties of $Li_{0.69}MnO_2$

The O2-type $Li_{0.69}MnO_2$ is a triclinic $Li_{0.69}MnO_2$ layered structure with space group $P6_3/mmc$. Its production involves utilizing the ion exchange method, where $Li_{0.69}MnO_2$ is derived through the exchange of Li^+ ions with the $Na_{0.69}MnO_2$ analogue in molten salt. Notably, both O2-type $Li_{0.69}MnO_2$ and $Li_{0.7}MnO_2$ do not undergo a transformation into a spinel structure during charging and discharging cycles [24]. The ion exchange technique is versatile and can be employed to generate various compounds with lithium-deficient stoichiometry. By exchanging Li^+ ions with the $Na_{0.7}MnO_2$ analogue in molten lithium salt, $Li_{0.7}MnO_2$ analogues are produced. In the $Na_{0.7}MnO_2$, oxygen ion sheet stacking defects are present, and after ion exchange, $Li_{0.7}MnO_2$ partially replaces these defects [24].

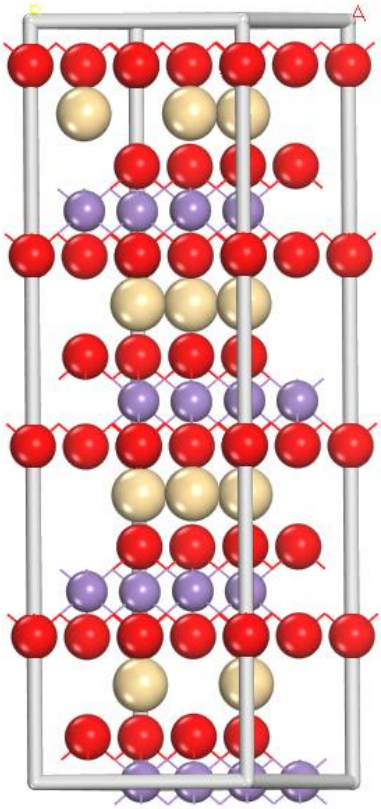

Figure 1.4. The triclinic crystal structure of $Li_{0.69}MnO_2$.

1.3.4. Coating

Over the past few decades, lithium-ion batteries have been the main source of energy storage and to this day they still are the leading technology for powering portable devices, consumer electronics, and electric vehicles [25]. These batteries are known for their high energy density, high power density, and long life cycle. Despite these great qualities, these batteries still have a few drawbacks such as capacity face and irreversible side reactions between the electrolyte and electrode material. Over the years researchers have investigated various ways of improving these drawbacks. These include elemental doping and cathode surface modification based on the coating technique [8]. The cathode surface modification based on the coating technique has been recently used to improve the electrochemical performance of various cathode materials by increasing their conductivity, improving their physical structures, and preventing reactions between the electrode material and electrolyte [26].

One such study was conducted by Jung and colleagues where they reported on the synthesis of a carbon-coated lithium titanate (LTO) anode microsphere through a solid-state reaction employing a blend of TiO_2, Li_2CO_3, and pitch. Their results illustrated that superior anode materials could be obtained by manipulating synthesis and structure. However, achieving a consistent carbon layer on the active particle surface and restraining undesirable particle growth during annealing proves challenging due to the disparity between the carbon additive and the metal precursor involved. Consequently, this approach exhibits limited enhancement in electrochemical performance [27]. Li and colleagues reviewed the success of various surface coating for cathode materials in lithium-ion batteries and reported that for common cathode materials; their surface structures are of great importance to their electrochemical performance [28].

In terms of capacity fade mitigation in cathode materials, a study on the capacity fade of the $LiCoO_2$ material was carried out by Hu G and others based on the sol-gel method to coat the material with $Li[Li_{0.2}Mn_{0.6}Ni_{0.2}]O_2$. They reported that the coated $LiCoO_2$ exhibited a higher voltage performance compared to the $LiCoO_2$ without $Li[Li_{0.2}Mn_{0.6}Ni_{0.2}]O_2$ coating layer. Notably, the $Li[Li_{0.2}Mn_{0.6}Ni_{0.2}]O_2$ layer was also able to eradicate the dissolution of Co into the electrolyte [29].

1.3.5. Core-shell architecture

The core-shell architecture in lithium-ion batteries (LIBs) represents a distinctive design strategy aimed at enhancing the electrochemical performance of these energy storage devices. In a typical core-shell structure, the active material (core) is enveloped by a shell, which serves various purposes such as mitigating volume expansion, improving electrical conductivity, and providing a protective layer. This architecture is particularly employed in electrode materials to address challenges like capacity fading, poor cycling stability, and limited rate capability [30].

Shen and colleagues explored the development of core-shell nanostructured materials for high-power lithium-ion batteries. They enhanced the electric conductivity of $Li_4Ti_5O_{12}$ by applying a carbon shell. The optimized design of these core-shell nanostructures facilitated rapid kinetics for both lithium-ion and electron transport, resulting in high-power performance [31].

In another study, Chen et al. investigated crystalline SnO_2/amorphous TiO_2 core-shell nanostructures for high-performance lithium-ion batteries. They demonstrated the thoughtful design of these nanostructures, employing a hydrothermal technique for the crystalline SnO_2 core and atomic layer deposition for the amorphous TiO_2 shell. In the electrochemical process, the SnO_2/TiO_2 nanostructures exhibited outstanding performance, displaying a high reversible capacity of 1259 mAh g^{-1} at an 80-mAg^{-1} cycling rate. Even after 50 cycles, the capacity was still notable at 703 mAh g^{-1}. Regardless of cycling rates or the number of cycles, the Coulombic efficiency consistently maintained around 100%. The electrochemical performance of SnO_2/TiO_2 batteries surpassed that of SnO_2 batteries lacking the TiO_2 coating [32].

A microscale core-shell $Li[(Ni_{0.8}Co_{0.1}Mn_{0.1})_{0.8}(Ni_{0.5}Mn_{0.5})_{0.2}]O_2$ configuration synthesis was reported by Sun et al. in 2009. The study found that this material's advantage over traditional cathode material in terms of stability (i.e., temperature) and discharge capacity can be attributed to its core-shell-like arrangement [33]. Ju and Ryu (2010) also looked at the coprecipitation approach for the synthesis of $Li(Ni_{0.8}Co_{0.15}Al_{0.05})_{0.8}(Ni_{0.5}Mn_{0.5})_{0.2}O_2$ core-shell. In comparison to the core structure, the synthesized material exhibits improved thermal stability, cyclic performance, and safety as determined by XRD, SEM, FE-SEM, EIS, and DSC analysis. The shell was credited with the thermal stability because it prevented the lattice's oxygen from leaking out [34].

Noh et al. (2014) used the mechanochemical ball-milling process to create nanostructured $yLi_2MnO_3(1-y)$ $LiMO_2$ (M=Ni, Mn, and Co) core-shell materials. Their findings demonstrated that the synthesised material performed better than

the nickel-rich core material. They hypothesized that the core $LiMO_2$ (nickel-rich) is responsible for the high specific capacity, while the shell Li_2MnO_3 is responsible for cell stability by mitigating the nickel's deleterious influence on the material surface. Li et al. (2015) also revealed that the LLO core-shell material outperformed the core-only and shell-only materials in terms of electrochemical performance. The enhancement was also attributed to the balance of the core and shell material's strengths and limitations in the hybrid (core-shell) system [13].

1.4. Rationale

Common cathode materials made from the O3-type Li_2MnO_3 suffer lattice microcracks or strains which then affect their processing ability, electrochemical performance and cycling lifespan [18]. Considerable efforts have been dedicated to tackling these challenges, encompassing strategies such as elemental doping, surface coating, core-shell configurations, and various other approaches. Creating a core-shell model of O2 and O3-type structures is key to understanding the complexity of electrode materials in lithium-ion batteries (LIBs). Core-shell structures are known to influence the electrochemical performance of LIBs, impacting factors such as capacity, cycling stability, and rate capability [13].

Although a lot of work has been done on the Li_2MnO_3, very little work has been done focusing on the coating of the material. Nah and others reported a study on the mechanical synthesis of Li_2MnO_3 shell/$LiMO_2$ (M = Ni, Co, Mn) core-structured nanocomposites for lithium-ion batteries. They used the Li_2MnO_3 which was said to stabilise the nanoparticles as a shell for the $LiMO_2$ [13]. However, there has not been any work reported where the Li_2MnO_3 was utilized as the core material.

In this study, the Li_2MnO_3 nanosphere is coated with the O2-type $Li_{0.69}MnO_2$ in a core-shell architecture to overcome the structural transformations that occur during cycling. The initial approach will be to investigate the electronic properties of the material to aid in understanding the conductivity of the material before

coating. Ultimately, calculating voltage profiles for the core-shell electrode structure is essential for gaining insights into the electrochemical behaviour of lithium-ion batteries. Voltage profiles provide a detailed understanding of the charge/discharge processes, offering information on the stability and reversibility of the electrochemical reactions within the core-shell structure. This objective contributes to the overall comprehension of the battery's performance [35]. For the interest of this study, the voltage profiles will only be calculated on the bulk systems to minimise the workload.

The second approach will be the utilisation of molecular dynamics simulations to optimize the systems' operating conditions. The variability of simulation conditions, including timesteps, temperatures, and pressure, is essential for a comprehensive exploration of lithium-ion battery behaviour. By systematically varying these parameters, researchers can gain insights into the sensitivity of the system, providing a more robust and realistic simulation of battery performance under different conditions. The core-shell structure will be subjected to various simulation conditions using the molecular dynamics DL_POLY code to optimise its operation conditions and investigate the structural response to the different simulation conditions it will be subjected to. Importantly, the shell materials' compatibility with the core is also governed by its ability to enhance ionic diffusion while protecting the cathode material from structural deformation and transformation.

Diffusion transport properties in lithium-ion batteries are crucial in understanding and optimizing their electrochemical performance. Diffusion processes play a pivotal role in governing the rate capability, cycling stability, and overall efficiency of LIBs. Studying the diffusion of lithium ions within electrode materials and through electrolyte solutions provides insights into the kinetics of charge and discharge processes. This knowledge is essential for addressing challenges such as capacity fading and slow charge/discharge rates. The diffusion transport properties of the coated O3-type materials will shed some light on understanding the effects of the shell material on the core material [36]. Importantly, the shell

materials' compatibility with the core is also governed by its ability to enhance ionic diffusion while protecting the cathode material from structural deformation and transformation [37].

1.4.1. Aims

The aim of this study is to design a core-shell model using the O2-type $Li_{5/6}MnO_2$ material as a coat for the O3-type Li_2MnO_3 cathode material and investigate their ionic and electronic properties.

1.4.2. Objectives

The objectives of this study will be to:

I. Perform geometry optimization of the O2-type and O3-type bulk materials and calculate structural and electronic properties.
II. Delithiate the optimized O3-type Li_2MnO_3 material.
III. Perform geometry optimization on the delithiated structures of Li_2MnO_3 and calculate structural and electronic properties.
IV. Generate a core-shell model of O2 and O3-type structures.
V. Vary the simulation conditions, timesteps, temperatures, and pressure.
VI. Investigate the diffusion transport properties for coated O3-type material.
VII. Calculate the voltage profiles for the core-shell electrode structure.

1.5. Outline

Chapter 1 deals with the general introduction of lithium-ion batteries and provides a brief overview of the operation of lithium-ion batteries. It further addresses the challenges faced by the current lithium-ion batteries. Moreover, the structural properties of our parent materials are discussed and outline the overall importance of the study.

Chapter 2 provides, in-depth, the theoretical aspects of the methodologies adopted in this study. It explains computational methods such as structure optimization, electronic properties calculations, formation energies and molecular dynamics methods.

Chapter 3 explains in detail the delithiation process of the core Li_2MnO_3 material. It explains the structure optimization of the O2 and O3-type materials and the structural and electronic properties of the delithiated $Li_{2-x}MnO_3$ ($0 \leq x \leq 1$) materials using density functional theory as implemented in the Vienna Ab Initio Simulation package (VASP) and the Cambridge Sequential Total Energy Package (CASTEP).

Chapter 4 explores the generation of core-shell systems through the MedeA interface, the use of molecular dynamics to optimize the simulation conditions of the generated core-shell systems, and studies of temperature effects on the systems.

Chapter 5 provides the conclusion of the whole study.

CHAPTER 2

METHODOLOGY

This chapter presents an overview of the methods employed in this study. The study uses classical molecular dynamics (MD) simulation-based methods and the density functional theory (DFT) within the Cambridge Serial Total Energy Package program (CASTEP) code and the Vienna Ab-initio Simulation Package (VASP) code. The relevant theory pertaining to classical molecular dynamics and quantum mechanics is presented in the following sections.

2.1. The Schrödinger Equation

The properties of materials comprising atoms or molecules can be obtained by solving the Schrödinger equation. The solution of the non-relativistic Schrödinger equation for an atomic or molecular system consisting of M nuclei and N electrons in the Born-Oppenheimer approximation is given by:

$$\hat{H}\psi = E\psi \tag{2.1}$$

where $\psi = \psi(r_1, r_2, \dots, r_N)$ is the wave function, E is the electronic energy and $\hat{H}$ is the electronic Hamiltonian. The electronic Hamiltonian can be expressed as

$$\hat{H} = \hat{T} + V_{ne} + V_{ee} \tag{2.2}$$

where

$$\hat{T} = -\sum_{i=1}^{N} \left(\frac{\nabla_i^2}{2}\right) \tag{2.3}$$

is the kinetic energy operator,

$$V_{ne} = \sum_{i=1}^{N} v(\boldsymbol{r}_i) \tag{2.4}$$

is the potential energy operator, and

$$V_{ee} = \sum_{i=1}^{N} \sum_{j>i}^{N} \frac{1}{|\boldsymbol{r}_i - \boldsymbol{r}_j|} \quad 2.5$$

is the electron-electron repulsion energy operator. The sum of the electronic energy E and the nuclear repulsion energy

$$V_{nn} = \sum_{a=1}^{M} \sum_{b>a}^{M} \frac{Z_a Z_b}{\boldsymbol{r}_{ab}} \quad 2.6$$

constitute the total energy of the system

$$E_{tot} = E + V_{nn} \quad 2.7$$

2.2. Density Functional Theory

Density Functional Theory (DFT) is an ab-initio quantum mechanical approach employed to compute the properties of atomic or molecular systems by solving the Schrödinger equation. The theoretical basis of DFT can be traced back to the Thomas-Fermi model, and its validity is confirmed by the Hohenberg-Kohn (H-K) theorems [38]. According to the first H-K theorem, the ground state features of a system with multiple electrons are exclusively dictated by an electron density that relies on just three spatial coordinates:

$$E = E\,[\rho(\boldsymbol{r})] \quad 2.8$$

In this context, E represents the ground-state energy, and ρ signifies the ground-state density of the system. This simplification addresses the intricate challenge of N electrons with 3N spatial coordinates by utilizing the electron density functional, condensing the problem to three coordinates. The ground state density also governs the external potential $v(\boldsymbol{r})$. The theorem's applicability extends to the time-independent domain, leading to a functional theory of time-dependent density used to describe excited states [38]. The initial Hohenberg-Kohn theorem establishes that all characteristics of the ground state for the system are determined solely by its density.

The second H-K theorem asserts the existence of a variation principle for the ground-state energy functional $E[\rho]$, indicating an inequality when ρ' deviates from the ground density:

$$E = E[\rho(\boldsymbol{r})] \leq E[\rho'(\boldsymbol{r})] \quad 2.9$$

Hohenberg and Kohn formulated the electronic energy in relation to a functional $F[p(\boldsymbol{r})]$ and this functional is independent of the potential $v(\boldsymbol{r})$ within the system, maintaining a consistent form across all systems:

$$E = F[\rho(\boldsymbol{r})] + \int \rho(\boldsymbol{r}) v(\boldsymbol{r}) d^3\boldsymbol{r} \quad 2.10$$

The latter term in the mentioned equation represents the potential energy arising from the attraction between the nucleus and electrons. $F[\rho(\boldsymbol{r})]$ is a universal functional that is unaffected by the potential v(r) of the system and maintains a consistent structure across all systems. This functional encompasses contributions from kinetic energy, classical Coulomb interaction, and a non-classical component.

$$F[\rho(\boldsymbol{r})] = T[\rho(\boldsymbol{r})] + J[\rho(\boldsymbol{r})] + E_{ncl}[\rho(\boldsymbol{r})] \quad 2.11$$

If $J[\rho(\boldsymbol{r})]$ is known, then the expressions for $T[\rho(\boldsymbol{r})]$ and $E_{ncl}[\rho(\boldsymbol{r})]$ need to be determined. The Thomas-Fermi model serves as an example of density functional theory, but its efficiency is compromised due to its inadequate approximation of kinetic energy. In Kohn-Sham (K-S) DFT, the complex issue of interacting electrons in static potentials is simplified by considering non-interacting electrons in an effective potential. This effective potential encompasses the internal potential and the effects of Coulomb interactions [39]. It includes the interactions between electrons in Coulomb, accounting for exchange and correlation effects, which are challenging to model within K-S DFT. Non-interacting systems, in contrast, are comparatively simpler. Kohn and Sham proposed calculating the kinetic energy of the non-interacting system with the same density as the interacting system [38], utilizing the following equations:

$$T_s = -\frac{1}{2}\int_i^N \langle \psi_i^*(\boldsymbol{r}) | \nabla^2 | \psi_i(\boldsymbol{r}) \rangle d\boldsymbol{r} \quad 2.12$$

$$\rho_s(\boldsymbol{r}) = \int_i^N \langle \psi_i(\boldsymbol{r}) \rangle |\psi_i(\boldsymbol{r_s})|^2 = \rho(\boldsymbol{r}) \quad 2.13$$

Therefore, ψ_i represents the non-interacting orbitals of the system, and T_s does not equate to the actual kinetic energy of the system. Following Kohn and Sham's approach, H-K introduced the separation of the functional $\mathrm{F}[\rho]$. Consequently, the Hohenberg-Kohn functional can be expressed with reference to the non-interacting kinetic energy:

$$F[\rho(\boldsymbol{r})] = T_s[\rho(\boldsymbol{r})] + J[\rho(\boldsymbol{r})] + E_{XC}[\rho(\boldsymbol{r})] \quad 2.14$$

where E_{XC} is the exchange-correlation energy, which can be defined by

$$E_{xc}[\rho(\boldsymbol{r})] = T[\rho(\boldsymbol{r})] - T_s[\rho(\boldsymbol{r})] + E_{ee}[\rho(\boldsymbol{r})] - J[\rho(\boldsymbol{r})] \quad 2.15$$

and

$$J[\rho(\boldsymbol{r})] = \frac{1}{2} \int d^3 r \int d^3 r' \frac{\rho(\boldsymbol{r})\rho(\boldsymbol{r'})}{|\boldsymbol{r}-\boldsymbol{r'}|} \quad 2.16$$

refers to the electrostatic energy arising from the charge distribution $\rho(\boldsymbol{r})$. By employing the variation principle and the second Hohenberg-Kohn theorem, one can derive the Kohn-Sham (K-S) equation in the form of a single-particle Schrödinger equation:

$$\left[-\frac{\nabla^2}{2} + v_s(\boldsymbol{r})\right] \phi_i(\boldsymbol{r}) = \varepsilon_i \phi_i(\boldsymbol{r}) \quad 2.17$$

where

$$v_s[\rho(\boldsymbol{r})] = v(\boldsymbol{r}) + \int d^3 \boldsymbol{r'} \frac{\rho(\boldsymbol{r'})}{|\boldsymbol{r}-\boldsymbol{r'}|} + v_{XC} \quad 2.18$$

If the electron density of the non-interacting systems matches that of the actual system, then the density for the N single-particle orbitals can be calculated as:

$$\rho(\boldsymbol{r}) = \rho_s(\boldsymbol{r}) = \sum_i^N |\phi(\boldsymbol{r})|^2 \quad 2.19$$

The exchange-correlation potential is obtained by taking the derivative of the exchange-correlation energy E_{XC} with respect to the electronic density $\rho(\boldsymbol{r})$:

$$v_{XC} = \frac{\delta E_{XC}[\rho(\boldsymbol{r})]}{\delta \rho(\boldsymbol{r})} \quad 2.20$$

Equations 2.16, 2.18, and 2.19 are widely recognized as the Kohn-Sham equations and have to be solved self-consistently.

2.2.1. Local Density Approximation

The practical application of the general expression for exchange-correlation energy, E_{XC}, is not feasible and requires approximation. The exchange-correlation energy in the local density approximation (LDA) is defined as:

$$E_{XC}^{LDA} = \int \epsilon_{XC}\big(\rho(\boldsymbol{r})\big)\rho(\boldsymbol{r})d\boldsymbol{r} \quad 2.21$$

Here, ϵ_{XC} represents the exchange-correlation energy per particle in a uniform electron gas with density ρ. This approximation is suitable for systems characterized by slowly changing and high-density conditions.

2.2.2. Generalized Gradient Approximation

The generalized gradient approximation (GGA) modifies the Kohn-Sham energy partitioning to acquire a non-local Hamiltonian, although it still possesses local characteristics [40]. The initial step towards the local density approximation (LDA) involves enhancing the density with the gradient of charge density information, $\nabla\, \rho(\boldsymbol{r})$, to accommodate the non-uniformity of the actual electron density.

Subsequently, the exchange-correlation energy, referred to as generalized gradient approximations, can be expressed as:

$$E_{XC}^{GGA}[\rho\alpha, \rho\beta] = \int f(\rho\alpha, \rho\beta, \nabla\rho\alpha, \nabla\rho\beta)d\boldsymbol{r} \quad 2.22$$

Alex Becke successfully introduced the hybrid functional in 1993 with the aim of enhancing the outcomes obtained through the exchange functional GGA:

$$E_{XC}^{hyb} = \alpha E_X^{KS} + (1-\alpha)E_{XC}^{GGA} \quad 2.23$$

In this context, E_X^{KS} represents the exchange calculated with the K-S wave function, E_{XC}^{GGA} denotes an appropriate GGA, and α stands for a fitting parameter [41]. The exchange-correlation energy within the generalized gradient approximation enhances the description of solids and atoms compared to the local spin density approximations (LSDA). This improvement is observed in total energies, structural energy differences, and the expansion and weakening of bonds [40]. GGA functions, particularly expressed in terms of Perdew-Wang, provide accurate and excellent results for molecular geometries and ground-state energies, potentially surpassing the accuracy of GGA and meta-GGA functions [40]. Other significant DFT functionals include Hybrid Meta GGA, hybrid, and double functionals, with GGA-PBE being an important exchange-correlation functional for solid-state calculations [42].

2.3. Projector Augmented Wave

This study utilizes the Projector Augmented Wave (PAW) method within the framework of Density Functional Theory (DFT), implemented in the CASTEP code, known for producing reliable results regarding the electronic and structural properties of various solids. The PAW method has proven successful and functions akin to pseudopotentials in many respects. While it shares a strong connection with ultra-soft pseudopotentials, it distinguishes itself by enabling the calculation of full wave functions, including core electron wave functions. In this approach, full wave functions undergo a transformation into auxiliary wave functions, which can be readily expanded in a plane wave basis. Simultaneously, the full wave functions are enriched with atomic wave functions. Although it operates under the assumption of the frozen-core approximation, the PAW method demonstrates superior transferability compared to pseudopotentials [43].

2.4. Plane Wave Pseudopotential Method

The plane-wave pseudopotential method is a technique employed for accurately computing the variational self-consistent solution within the framework of density

functional theory. It is particularly suitable for large systems governed by 3D periodic boundary conditions. In this approach, the wave function undergoes expansion using a plane-wave basis, providing an effective pseudopotential representation of the ions within the crystal.

2.4.1. Plane Wave Basis

Utilizing a plane wave basis set offers several advantages, including the simplicity of the basis function with no assumptions about the shape of the solution, the elimination of basis set superposition errors, and the ability to efficiently compute forces on atoms [44]. This approach requires expanding the electronic wave function of the system. The plane-wave pseudopotential method proves to be a reliable technique for investigating material properties. A clear demonstration of the plane-wave basis technique is provided through the application of Bloch's theorem [45]. Bloch's theorem allows electronic wave functions to be straightforwardly expanded using plane waves. The expression of electronic wave functions for periodic solids, as well as problems involving atoms and surfaces according to Bloch's theorem, can be formulated as follows:

$$\Psi_i(\boldsymbol{r}) = e^{[i\boldsymbol{k}.\boldsymbol{r}]} F_i(\boldsymbol{r}) \qquad 2.24$$

This enables us to express the wave functions of the crystal by expanding them in terms of plane waves, denoted as $F_i(\boldsymbol{r})$:

$$F_i(\boldsymbol{r}) = \Sigma_{G\rightarrow} C_i G e^{[i\boldsymbol{G}.\boldsymbol{r}]} \qquad 2.25$$

Therefore, G represents the reciprocal lattice vectors of the periodic cell. Subsequently, each electronic wave function can be articulated as follows:

$$\Psi_{ki}(\boldsymbol{r}) = \Sigma_G C_i, K + G\ e^{[i(K+G).\boldsymbol{r}]} \qquad 2.26$$

Here, $C_i, K + G$ denote the coefficients of plane waves, and they are entirely dependent on the specific kinetic energy.

$$\left(\frac{\hbar^2}{2m}\right) |K + G_c|^2 \qquad 2.27$$

The mentioned parameter governs the convergence of the expansion by determining the cut-off for kinetic energy. The plane-wave basis set is confined within a sphere in reciprocal space, expressed through an energy cut-off denoted as E_{cut}. For all values of G, the kinetic energies are restricted to be less than or equal to a specific cut-off energy, as outlined below:

$$\left(\frac{\hbar^2}{2m}\right)|K + G_c|^2 \leq E_{cut} \qquad 2.28$$

The selection of the energy cut-off involves incrementing its value until the total energy converges to the desired accuracy [43]. Increasing the plane wave number enables the description of more rapidly varying features, allowing for the potential achievement of an infinitely large basis set. Finite basis sets are obtained by introducing a finite cut-off energy to the discrete plane-wave basis set. To prevent errors in the computation of total energy, the cut-off energy should be increased until the calculated energy converges. The use of a denser set of k-points is essential to minimize errors and ensure robust convergence.

2.4.2. Pseudopotential Method

The pseudopotential method is a potent technique designed to replace the atomic all-electron potential effectively, eliminating core states and characterizing valence electrons through pseudo-wave functions. In the context of valence electrons navigating through a crystal, including relativistic effects, a weak pseudopotential is employed, which substitutes the electron core and the attractive Coulomb potential within the ionic core [38]. The pseudo-valence electron and pseudo-ion cores take the place of the original solid. The pseudo-electron experiences a milder potential within the core region but encounters the same potential outside the core region as the original electron. The ionic potential (Z/r), valence wave function (ψ_v), the corresponding pseudopotential V_{pseudo}, and pseudo-wave function (ψ_{pseudo}) are illustrated in Figure 2.1 [43]. The utilization of the pseudopotential approximation method offers an advantage, as it enables the electronic wave function to be expanded using a smaller number of plane-wave basis states. The most general form of pseudopotential is:

$$V_{NL} = \Sigma|lm\rangle V_i \langle lm| \qquad 2.30$$

In the given context, $|lm\rangle$ and $\langle lm|$ represent spherical harmonics, and V_i is the pseudopotential associated with angular momentum l. This operator, when applied to the electronic wave function, decomposes it into spherical harmonics, each multiplied by the relevant pseudopotential V_i. The local pseudopotential employs the same potential for all angular momentum components.

The plane-wave calculations utilize the ultra-soft pseudopotential developed by Vanderbilt [46]. Within this scheme, pseudo-wave functions are permitted to be soft within the core region. The ultra-soft pseudopotential (USP) extends its applicability to a broad range of atoms, including transition metals. In this report, we employ the USP for total energy calculations within the CASTEP program [47].

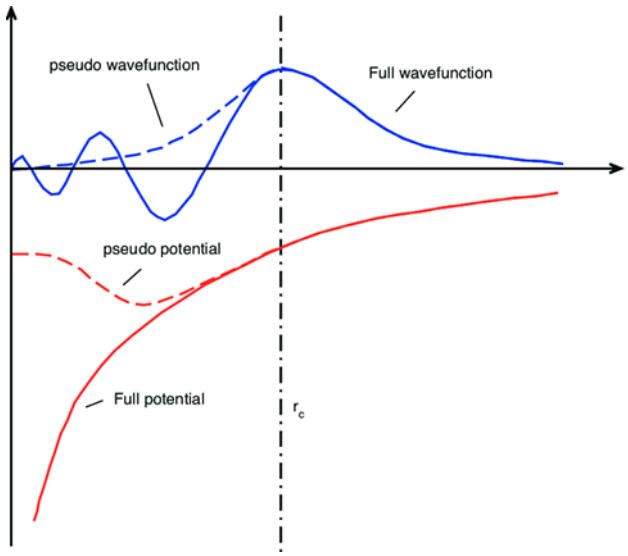

Figure 2.1. The comparison involves a wave in the Coulomb all-electron potential of the nucleus (solid blue and red lines) and the pseudopotential (blue and red dashed lines). The pseudo wave function, as well as the real and potential components, align at the specified radius r_c [43].

2.5. Classical Molecular Dynamics

Molecular dynamics (MD) simulation methods employ statistical mechanics to calculate the equilibrium and dynamic properties of a large-scale system. MD simulations offer a detailed atomic representation of the microstate of the system at a specific point in time and space. The atomic dynamics enable the determination of thermally accessible states for the system, influencing material behaviour and characteristics. The fundamental concept underlying MD involves the application of Newton's equation of motion to predict the spatial trajectory of a system under the influence of a specific force field [48, 49]. The classical equations of motion for a simple atomic system can be expressed as:

$$m_i \ddot{r}_i = f_i, \tag{2.31}$$

$$f_i = -\frac{\partial}{\partial r_i} \boldsymbol{u} \tag{2.32}$$

Here, r_i represents the three spatial coordinates of each atom, and m denotes the atomic mass. The potential energy $\mathcal{U}(r^N)$, where r^N represents the entire set of 3N atomic coordinates, is utilized to compute the forces acting on the atoms. The accuracy of the outcomes in molecular dynamics simulations, especially in describing the mechanical aspects of the structure, relies on the precision of the underlying force fields. To initiate an MD simulation, it is recommended to start with an ideal configuration corresponding to a minimum potential energy surface, as determined by experiments. The species are propelled at a velocity that maintains their kinetic energy E_k consistent with the desired temperature T. Utilizing the Equipartition Theorem at thermal equilibrium for each $\frac{k_B T}{2}$ normal mode, the expression can be written as:

$$< k_B > = \frac{1}{2} \sum_{i=1}^{3N} m_i v_i^2 \equiv \frac{1}{2} (V^0)^T M (V^0) = (N_F k_B T)/2, \tag{2.33}$$

where N_F represents the system's degrees of freedom.

2.5.1. The Potential Model

The potential model characterizes the energy of the system at a specific point and time by considering the atomic coordinates of the atomic species relative to their positions. The interatomic or intermolecular potentials are defined by a set of analytical functions, with appropriate input parameters obtained by fitting these functions to experimentally derived lattice features such as lattice constants. This approximation of atomic or molecular potential, employed in molecular dynamics or Monte Carlo simulations, overcomes the limitation on system size encountered by quantum mechanics-based electronic structure approaches. A molecular dynamics simulation, utilizing numerical methods to calculate the system's parameters, can effectively track the behaviour of a system comprising numerous atoms.

i) Buckingham Potential

The Buckingham potential, formulated by Richard Buckingham, mathematically delineates the potential experienced by two interacting atoms beyond their bond length. This potential function accounts for van der Waals energy and incorporates the Pauli Exclusion Principle. Richard Buckingham employed an exponential function to depict repulsion, with increasing strength for values of the interatomic distance r less than the bond length. The Buckingham potential is articulated as:

$$V(r) = Ae^{-Br} - \frac{\lambda}{r^6} \qquad 2.34$$

In this expression, Ae^{-Br} denotes the nuclear-nuclear repulsion, and the $-\frac{\lambda}{r^6}$ signifies the attractive component, thereby contributing to the depiction of the bond length between the interacting atoms [50]. The Buckingham potential finds extensive use in numerous large-scale atomistic simulations, producing results comparable to experimental findings. Nevertheless, this potential falls short in describing interactions occurring at near-zero separation. This limitation arises

because the exponential part of the Buckingham potential reaches a finite value as r approaches zero, while the attraction term extends to infinity. Molecular dynamics simulation codes like DL_POLY [51] , which employ this potential function, are designed to identify such conditions and automatically prevent their unphysical nature at separation values near zero.

ii) Lennard-Jones Potentials

Another commonly used potential function in Monte Carlo or Molecular Dynamics simulations is the Lennard-Jones potential, often expressed as:

$$V(r) = 4\epsilon\left[\left(\frac{\sigma}{r}\right)^{12} - \left(\frac{\sigma}{r}\right)^{6}\right] \quad 2.35$$

or as expressed as:

$$V(r) = \frac{A}{r^{12}} - \frac{B}{r^{6}} \quad 2.36$$

In this expression, ϵ signifies the bond strength between the two atoms, and σ represents the value of r at which V becomes zero. The London dispersion forces are determined by the $-\frac{B}{r^6}$ term, while the nuclei-nuclei repulsion is characterized by the $\frac{A}{r^{12}}$ term. The values of A and B are specific to the atoms being studied and are determined through fitting to experimental data.

iii) Born Model of Ionic Solids

In classical simulations, a crystal is conceptualized as a collection of formally charged ionic spheres with an infinite atomic arrangement. This perspective aligns with the Born model of ionic solids, allowing such crystals to be characterized using a potential model. In this model, the interatomic or intermolecular potential between interacting atoms or molecules is articulated as a function of their atomic positions. The energy arising from the interaction between two ionic spheres treated as point charges is determined by:

$$U_{ij} = \frac{1}{4\pi\varepsilon}\frac{q_i q_j}{rij} + \phi(r_{ij}) \quad 2.37$$

In this expression, U_{ij} represents the overall Coulombic interaction resulting from the interaction between the ionic spheres, with $\phi(r_{ij})$ indicating the short-range interaction. Additionally, ε denotes the permittivity of the vacuum, q_i and q_j signify the point charges representing the ionic spheres, and r_{ij} is the separation distance. The precision of the outcomes relies on the short-range interaction, as the electrostatic energy is pre-determined [52, 53].

2.5.2. Statistical Ensembles

The complex systems of statistical mechanics exhibit a diverse array of properties contingent on the system's state at a particular moment. These states, equally likely and characterized by specific properties based on imposed constraints, represent snapshots of the system. These snapshots, known as ensembles, are a prerequisite for invoking the probability function. Within a statistical ensemble, it becomes possible to regulate thermodynamic properties such as energy, temperature, and pressure to achieve a desired simulation environment. In this study, we utilize the constant-energy, constant-volume (NVE), constant-temperature, constant-volume (NVT), constant-temperature, constant-pressure (NPT), and constant-temperature, constant-stress (NST) ensembles.

i) The NVE Ensemble

The constant-energy, constant-volume ensemble (NVE), also known as the microcanonical ensemble, is generated by solving Newton's equations without considering temperature or pressure. In this ensemble, energy is conserved, but a slight energy drift may occur due to rounding and truncation errors during the integration process. The Verlet leapfrog algorithm is employed, where only $r(t)$ and $v(1-\frac{1}{2}at)$ are known at each timestep, leading to potential and kinetic energies being half a step out of synchrony. While the difference in kinetic energies is minor, it contributes to overall energy fluctuations.

Constant-energy simulations are not recommended for equilibration since achieving the desired temperature requires the energy flow facilitated by temperature control methods. However, this ensemble is valuable for exploring the constant-energy surface of conformational space during data collection or when avoiding temperature- and pressure-bath coupling perturbations for specific reasons [54, 55, 56].

ii) The NVT Ensemble

The constant-temperature, constant-volume ensemble (NVT), is also known as the canonical ensemble. This ensemble is established by controlling the temperature during the initialization stage through direct temperature scaling and temperature-bath coupling during the data collection stage. Throughout the simulation, the volume remains constant. This ensemble is particularly suitable for conformational searches on molecules in a vacuum without periodic boundary conditions, where volume, pressure, and density are not defined. Constant-pressure dynamics are not achievable in the absence of periodic boundary conditions. Even with periodic boundary conditions, the constant-temperature constant-volume ensemble offers the advantage of less trajectory perturbation due to the absence of coupling to a pressure bath [54, 55, 56].

iii) The NPT Ensemble

The NPT ensemble, characterized by constant temperature and pressure conditions, allows for simultaneous control of both temperature and pressure. In this ensemble, the unit cell vectors are flexible, and pressure is adjusted by modifying the volume. When precise regulation of pressure, volume, and densities is essential for the simulation, the NPT ensemble is the preferred option. Additionally, this ensemble can be used to achieve the desired temperature and pressure before transitioning to the constant-volume or constant-energy ensemble during the data collection phase [54, 55, 56].

iv) The NST Ensemble

The constant-temperature, constant-stress ensemble (NST) is an extension of the constant-pressure ensemble. Along with the isotropically applied hydrostatic pressure, the constant-stress ensemble enables control over the xx, yy, zz, xy, yz, and zx components of the stress tensor, also referred to as the pressure tensor. This ensemble is particularly valuable for investigating the stress-strain relationship in polymeric or metallic materials [54, 55, 56].

2.6. Simulation Codes

2.6.1. CASTEP Code

The Cambridge Serial Total Energy Package (CASTEP) program [57] is a quantum mechanical code based on first principles that investigates the properties of crystals and surfaces, allowing the simulation of a broad range of materials, including surfaces, crystalline solids, and various molecules. The program is capable of both single-point energy calculations and geometry optimization. The plane-wave (PBE) pseudopotential method using the generalized gradient approximation of Perdew-Burke Ernzerhof 1991 (GGAPW91) [41] was utilized.

2.6.2. VASP Code

The Vienna Ab-initio Simulation Package (VASP) is a solid-state electronic program that employs the plane-wave basis set, pseudopotentials, and the projected augmented wave method for conducting ab-initio quantum mechanical molecular dynamics. While grounded in the density functional theory (DFT) method, VASP also supports hybrid functional mixing DFT, Hartree-Fock exchange, the many-body perturbation theorem, and electronic corrections within a random phase approximation [213]. The program utilizes effective matrix

diagonalization schemes and Pulay/Broyden charge density mixing, employing advanced techniques to circumvent issues associated with the original Car-Parrinello method, which integrates electronic and ionic equations of motion simultaneously. The PAW method or ultra-soft Vanderbilt pseudopotential (US-PP) [214] is employed to describe the interaction between ions and electrons. For transition metals and first-row elements, ultra-soft pseudopotentials and projector-augmented waves allow a substantial reduction in the number of plane waves per atom. VASP can calculate forces and the full stress tensor, enabling the relaxation of atoms into their instantaneous ground state. Additionally, VASP is utilized for calculating state densities. Developed by M. Payne [200] at MIT, VASP shares its roots with the CASTEP/CETEP code but diverged from it in its early development.

CHAPTER 3

FIRST PRINCIPLE STUDY ON DELITHIATION OF Li_2MnO_3

3.1. Introduction

The Li_2MnO_3 suffers its intrinsic structural instability, leading to capacity fading and reduced cycling stability during charge and discharge processes. Additionally, the voltage decay associated with this cathode can compromise the overall performance of the battery. Its susceptibility to oxygen release and transition metal dissolution further contributes to capacity degradation and poses safety concerns [58]. These challenges emphasize the need for comprehensive research and development efforts to address and mitigate the limitations associated with Li_2MnO_3 when used as a cathode material in lithium-ion batteries. This chapter explores the structural and electronic properties during the delithiation process of $Li_{2-x}MnO_3$ where $0 \leq x \leq 1$. Furthermore, it presents the results and the discussion on the structural properties of the O2-type $Li_{0.69}MnO_2$ and structural and electronic properties of the O3-type Li_2MnO_3 bulk and the delithiated materials using the density of states as implemented in Vienna Ab Initio Simulation Package (VASP) and CASTEP codes. The density of states helps us analyse the physical properties and stability of the materials based on their electron contributions at the fermi level, and the electronic band structures provide insight into the conductivity of the materials.

3.2. Simulation procedure

Calculations for O2-type $Li_{0.69}MnO_2$ in this chapter were performed using the density functional theory framework in the CASTEP code due to its efficiency with a large number of atoms and employing the Perdew-Burke-Ernzerhof (PBE) exchange-correlation functional within the generalized gradient approximation framework (GGA). Calculations for the O3-type Li_2MnO_3 bulk and delithiated $Li_{1.75}MnO_3$, $Li_{1.5}MnO_3$, $Li_{1.25}MnO_3$, and Li_1MnO_3 materials were performed using

the density functional theory framework in the VASP code employing the Perdew-Burke-Ernzerhof (PBE) exchange-correlation functional within the generalized gradient approximation framework (GGA). The selection of cutoff energy and k-point mesh was conducted through convergence tests in which single-point energy calculations were performed where the cutoff energy or k-points were varied while the k-points or cutoff energy were kept constant, respectively. The chosen values were 500 eV and 5x5x5 for the O2-type material and 500 eV and 4x4x4 for the O3-type material. These parameters were applied for geometry optimization and the calculation of structural and electronic properties. Detailed discussions on the results of convergence tests are provided in the following subsections.

3.2.1. Cutoff energy

Figure 3.1 illustrates the results of the convergence test for the cut-off energy applied to $Li_{0.69}MnO_2$ and Li_2MnO_3. In Figure 3.1(a), the cut-off energy convergence for $Li_{0.69}MnO_2$ is presented. The graph reveals that the total energy experienced a notable decrease from 200 eV, with the highest total energy observed at 100 eV. A consistent trend emerged from the cut-off energy of 500 eV, indicating that the total energy of the system began to converge at this point. Similarly, Figure 3.1(b) for Li_2MnO_3 demonstrated that the total energy of the system also converged at a cut-off energy of 500 eV. This value was chosen as the optimal cut-off energy for structure optimization, as it was determined to be sufficient for achieving convergence in the total energy of both systems.

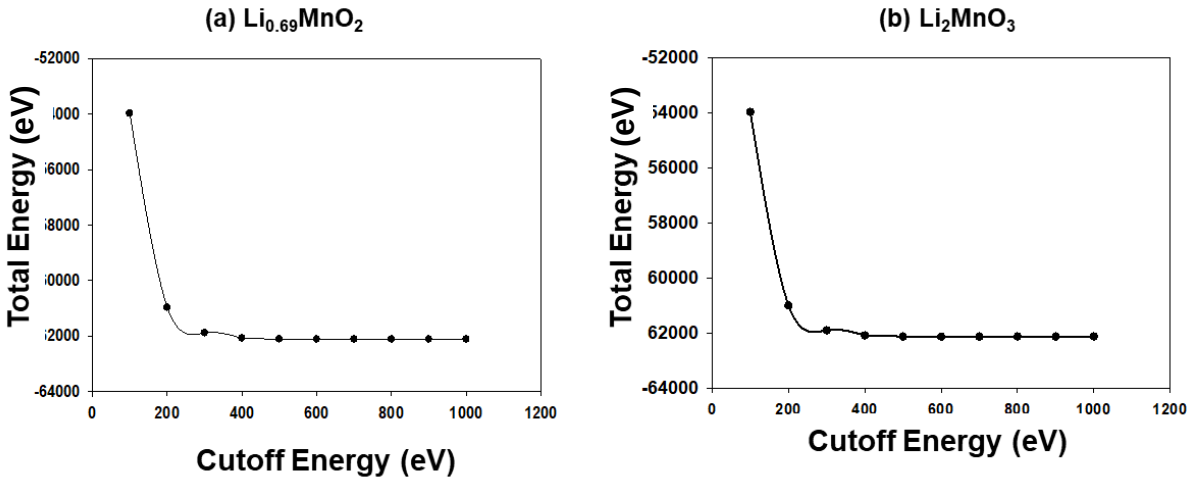

Figure 3.1. The cut-off energy convergence tests for (a) $Li_{0.69}MnO_2$ and (b) Li_2MnO_3 cathode materials.

3.2.2. K-Points

Figure 3.2 illustrates the k-point mesh sampling for both $Li_{0.69}MnO_2$ and Li_2MnO_3. In Figure 3.2(a), the k-point mesh sampling for $Li_{0.69}MnO_2$ is depicted. The graph indicates that the 1x1x1 k-point configuration resulted in the lowest total energy, followed by a rapid increase in total energy, with the 3x3x3 k-point configuration exhibiting the highest total energy. Subsequently, the total energy of the system stabilized consistently from the 5x5x5 k-point mesh. In contrast, Figure 3.2(b) demonstrates the k-point sampling for Li_2MnO_3. Unlike $Li_{0.69}MnO_2$, the 1x1x1 k-point configuration showed the highest total energy, which then rapidly decreased at the 2x2x2 k-point configuration. Additionally, the total energy of the system exhibited a steady trend from the 4x4x4 k-point mesh. Consequently, the k-point meshes of 5x5x5 and 6x6x6 were selected for $Li_{0.69}MnO_2$ and Li_2MnO_3, respectively.

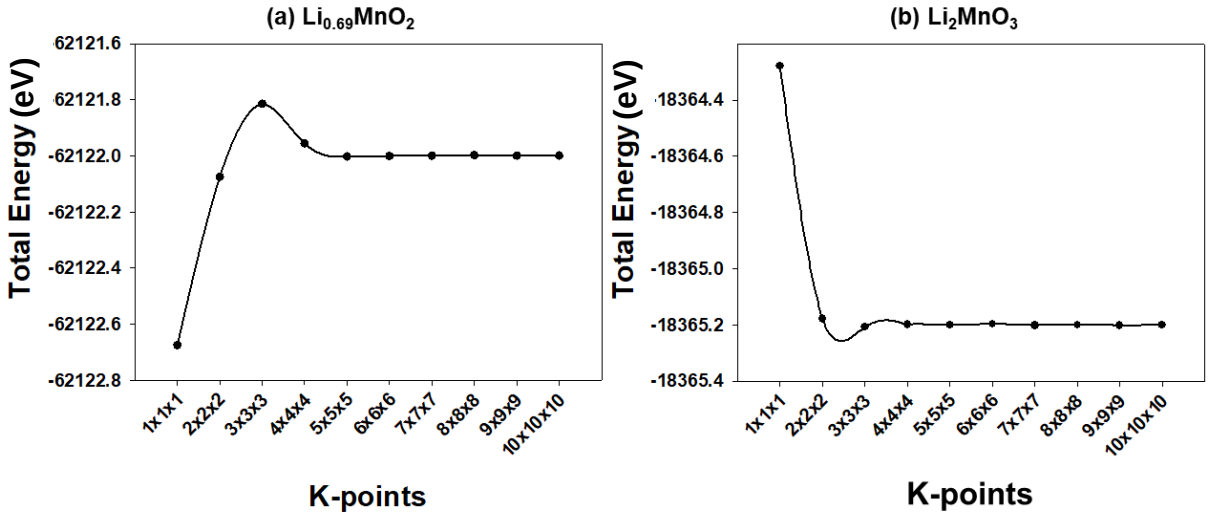

Figure 3.2. The k-point mesh convergence tests for (a) $Li_{0.69}MnO_2$ and (b) Li_2MnO_3 cathode materials.

3.3. Optimization of O2-$Li_{0.69}MnO_2$ and O3-Li_2MnO_3

A cutoff energy of 500 eV and a k-point mesh of 6x6x6 were selected for the O2-type $Li_{0.69}MnO_2$ material as they proved adequate for converging the total energy of the system. For the O3-type Li_2MnO_3 bulk and delithiated $Li_{1.75}MnO_3$, $Li_{1.5}MnO_3$, $Li_{1.25}MnO_3$, and Li_1MnO_3 materials, a cutoff energy of 500 eV and a k-point mesh of 4x4x4 were chosen for calculating the properties of both the bulk material and the delithiated materials, as they were determined to be sufficient for convergence of the system.

3.3.1. Structural properties of Li_2MnO_3 and $Li_{0.69}MnO_2$

Figure 3.3 and Table 3.1 below depict crystal structures and structural properties of the O2-type $Li_{0.69}MnO_2$ and O3-type Li_2MnO_3 materials. Figure 3.3 showcases the monoclinic crystal structure of Li_2MnO_3 and the triclinic crystal structure of $Li_{0.69}MnO_2$. Meanwhile, Table 3.1 presents the calculated lattice parameters in comparison to those reported in the literature. The calculated lattice parameters align well with the values previously documented in the literature with a percentage difference for the Li_2MnO_3 of a ≈ 1.21%, b ≈ 1.22%, and c ≈ 0.87%

and a percentage difference for $Li_{0.69}MnO_2$ of a ≈ 2.50%, b ≈ 2.57%, and c ≈ 4.75%.

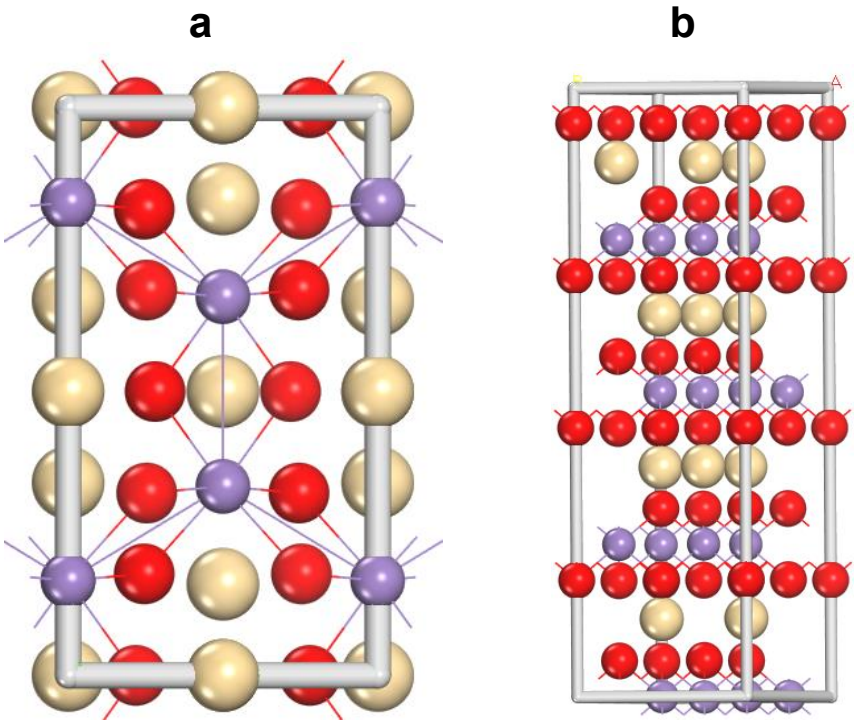

Figure 3.3. The crystal structures of (a) monoclinic Li_2MnO_3 and (b) triclinic $Li_{0.69}MnO_2$.

Table 3.1. Structural properties of O2-$Li_{0.69}MnO_2$ and O3-Li_2MnO_3.

Structures		Lattice parameters			Volume (Å)³
		a (Å)	b (Å)	c (Å)	
Li_2MnO_3	This work	4.997	8.637	5.074	51.601
	Reference [59]	4.937	8.532	5.030	
	% Difference	1.21	1.22	0.87	
$Li_{0.69}MnO_2$ **$Li_x[Li_{1/4}Mn_{3/4}]O_2$**	This work	2.772	2.770	10.254	66.996
	Reference [60]	2.842	2.842	9.778	
	% Difference	2.50	2.57	4.75	

3.3.2. Electronic and mechanical properties of $Li_{0.69}MnO_2$ and Li_2MnO_3

The electronic band structures of $Li_{0.69}MnO_2$ and Li_2MnO_3 are presented in Figures 3.4 and 3.5 below, respectively. Figure 3.4 displays the electronic band structure of $Li_{0.69}MnO_2$, revealing a band gap of zero at the Fermi level, indicating the material's metallic nature. In Figure 3.5, the electronic band structure of Li_2MnO_3 is depicted, showcasing the material as a magnetic semiconductor with an indirect band gap of 1.781 eV. The valence band maximum is situated at 0.039 eV relative to the Fermi level, and the conduction band is positioned at 1.820 eV relative to the Fermi level. The band gap was determined by employing the spin-polarized local density approximation, with a Hubbard U parameter set at 5. This selection was made because it yielded a band gap estimate that closely matched the value documented in literature.

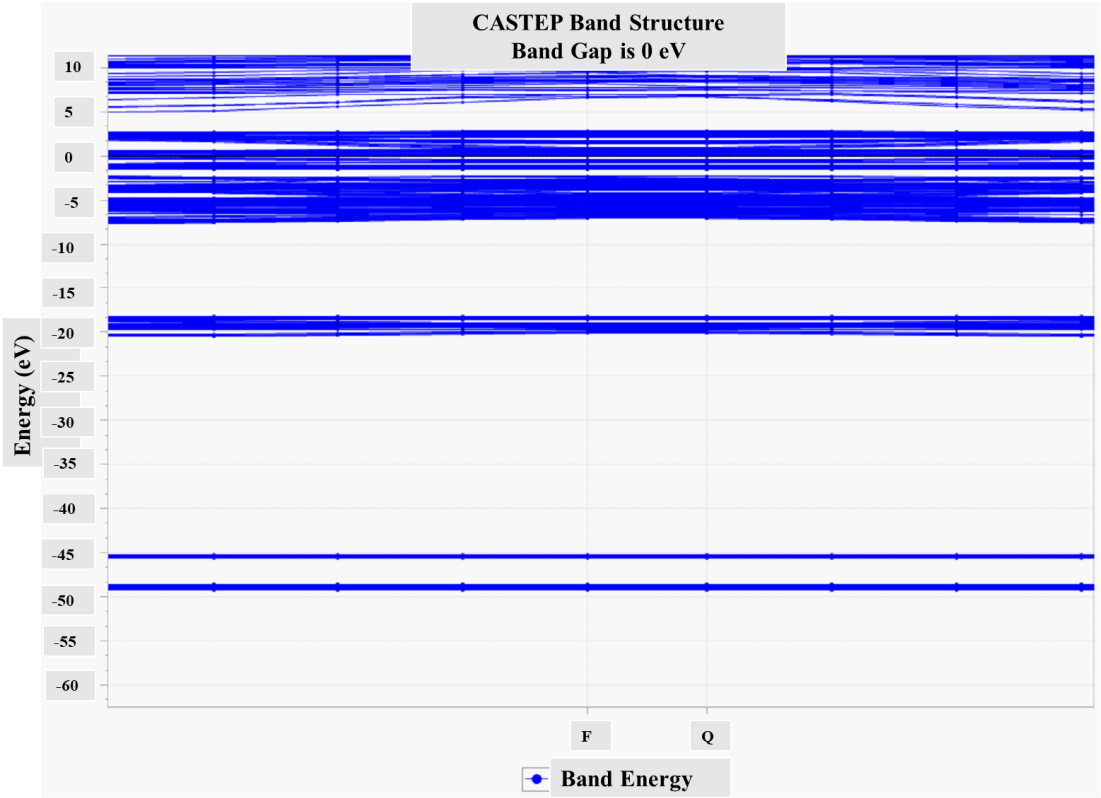

Figure 3.4. The electronic band structure of $Li_{0.69}MnO_2$ cathode material.

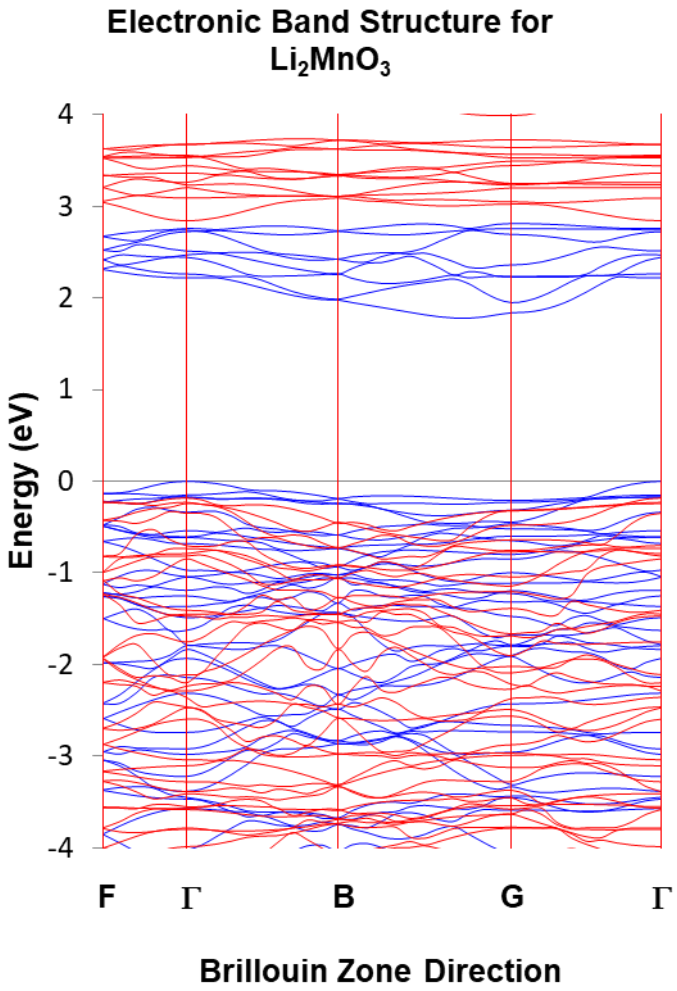

Figure 3.5. The electronic band structure of Li_2MnO_3 cathode material.

Figures 3.6 and 3.7 below depict the partial and total density of states for the O2 and O3-type materials. In Figure 3.6, illustrating $Li_{0.69}MnO_2$, the electron contribution at the Fermi level arises from the p state of oxygen and the d state of manganese. The total density of states displays a pronounced peak at the Fermi level, indicating the material's metallic nature. Figure 3.7 displays the partial and total density of states (PDOS and TDOS) for the Li_2MnO_3 material. Examining the partial density of states, it is evident that lithium makes a minimal contribution to the material's density of states (DOS), whereas, for manganese, the PDOS is predominantly influenced by the d states of the atom. Additionally, the PDOS for the oxygen atom is significantly impacted by the p states of the atom. Furthermore, the d states of manganese exhibit a substantial contribution to the conduction band and some contribution to the valence band at the Fermi

level of the TDOS for the material. No electron overlap was observed at the Fermi level of the TDOS for Li_2MnO_3. The absence of electron overlap at the Fermi level results in a band gap of 1.781 eV, which closely aligns with the reported band gap of 1.68 eV by Shuo Wang and colleagues. The existence of this band gap at the Fermi level indicates a semiconductor behaviour.

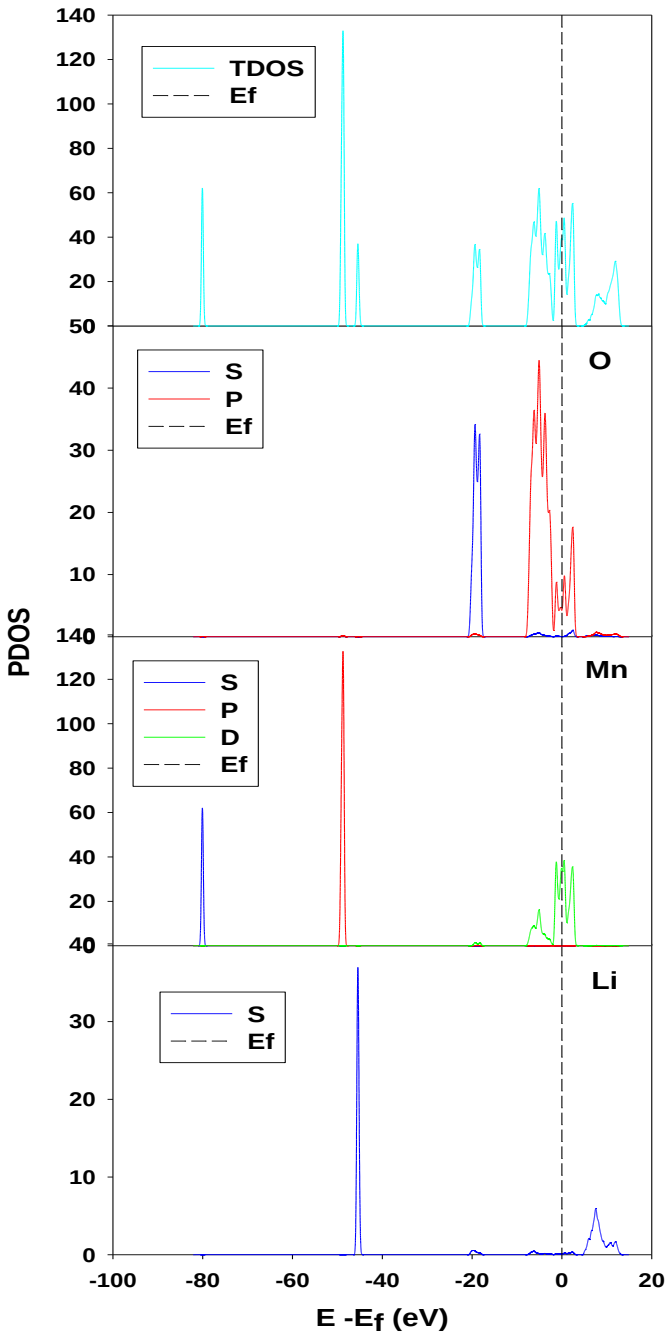

Figure 3.6. The partial and total density of states of $Li_{0.69}MnO_2$.

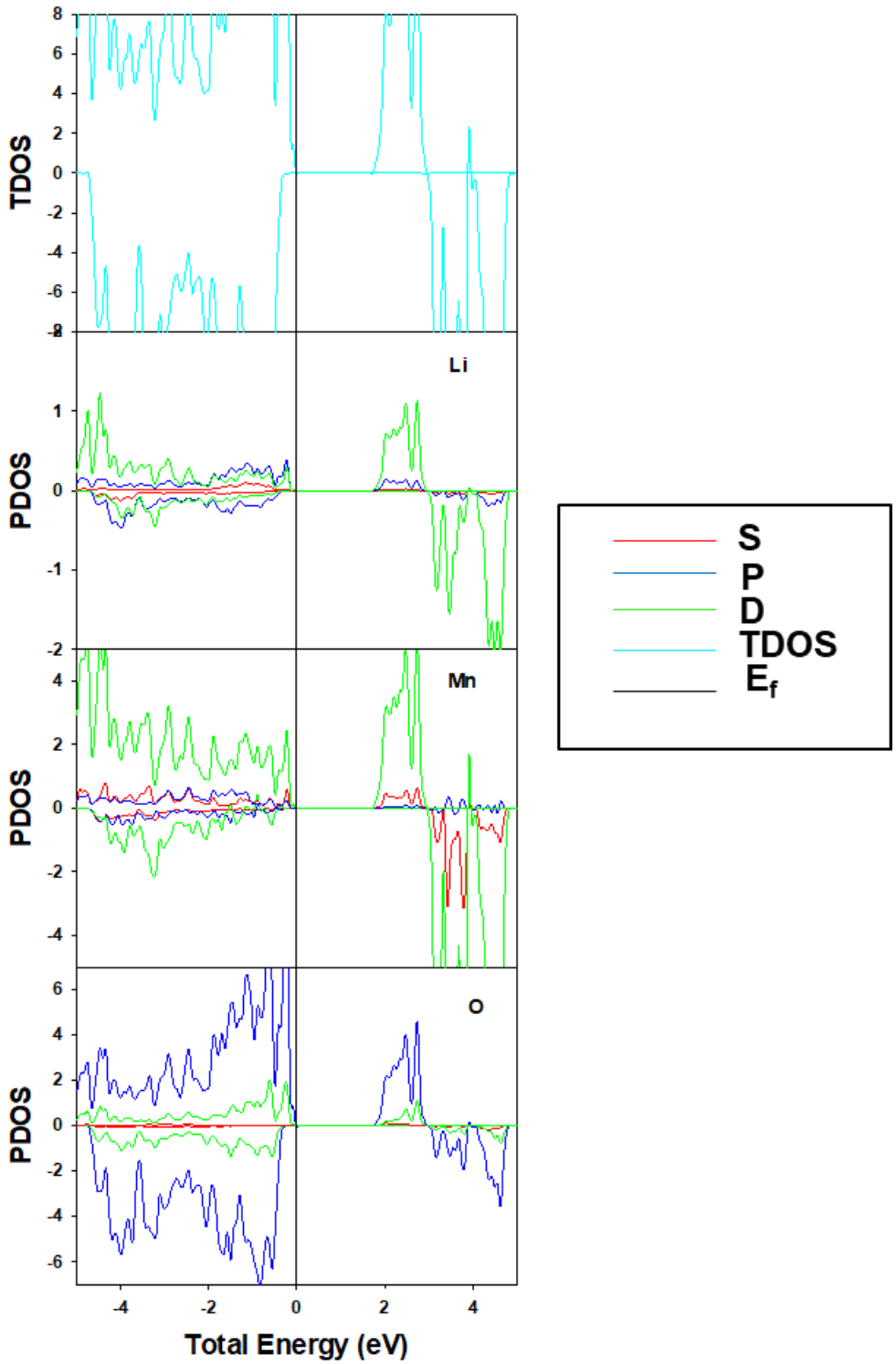

Figure 3.7. The partial and total density of states of Li_2MnO_3 in a spin-polarised configuration.

3.4. Delithiation process of $Li_{2-x}MnO_3$

3.4.1. Structural properties

Figure 3.8 shows the delithiated $Li_{2-x}MnO_3$ structures. The lithium vacancies in the material $Li_{1.75}MnO_3$, $Li_{1.5}MnO_3$, $Li_{1.25}MnO_3$, and Li_1MnO_3 materials were randomly created. The lithium vacancies were made at the 2c sites for the $Li_{1.75}MnO_3$, at the 2b, 2c, and 4h sites for $Li_{1.5}MnO_3$, at the 2c and 4h sites for $Li_{1.25}MnO_3$, and finally, at the 2b, 2c, and 4h sites for the Li_1MnO_3. Table 3.2 below shows the calculated lattice parameters and formation energies of the delithiated structures, $Li_{1.75}MnO_3$, $Li_{1.5}MnO_3$, $Li_{1.25}MnO_3$, and Li_1MnO_3 structures. The lattice parameters of the materials were found to be comparable to the lattice parameters of the parent material Li_2MnO_3. Based on the calculated lattice parameters, the crystal structures were found to be monoclinic with space group C2/m.

i) Crystal structures

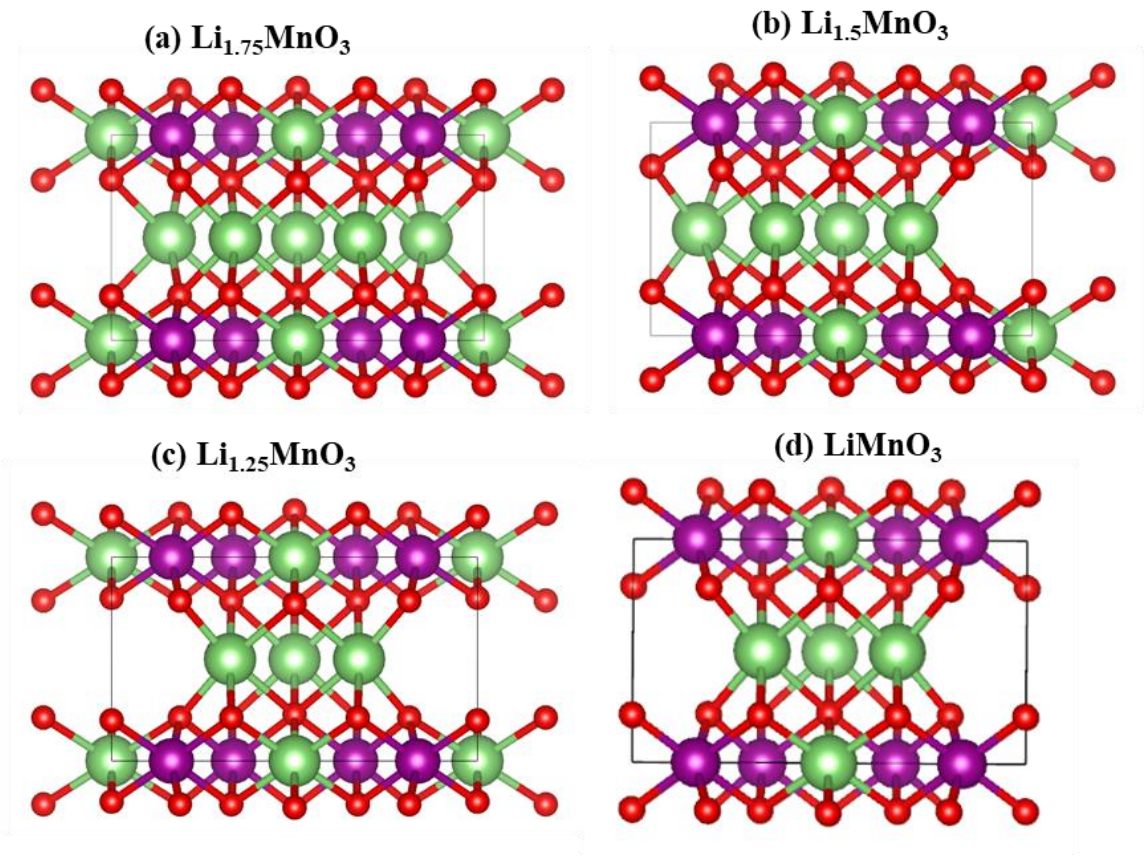

Figure 3.8. The delithiated $Li_{2-x}MnO_3$ structures (a) $Li_{1.75}MnO_3$, (b) $Li_{1.5}MnO_3$, (c) $Li_{1.25}MnO_3$, and (d) $LiMnO_3$.

Table 3.2. The structural properties and formation energies for the delithiated $Li_{2-x}MnO_3$ structures.

Materials	Lattice parameters			Formation energy
	a (Å)	b (Å)	c (Å)	KJ/mol
$LiMnO_3$	4.957 Å	8.673 Å	5.151 Å	-204.195
$Li_{1.25}MnO_3$	5.009 Å	8.716 Å	5.128 Å	-935.648
$Li_{1.5}MnO_3$	4.981 Å	8.676 Å	5.103 Å	-524.562
$Li_{1.75}MnO_3$	4.960 Å	8.710 Å	5.071 Å	-1161.594

ii) Vacancy formation and energy of formation

Figure 3.9 below shows the plots for the vacancy formation energy and the energy of formation against the lithium concentration. The vacancy formation plot indicated an increasing trend alluding that the increase in the number of lithium being removed from the system increases the amount of energy required to create these vacancies. In contrast, the plot for the energy of formation against the concentration of the lithium indicated a fluctuating curve during the charging process since the delithiation process was randomly done and different energies are required to remove the lithium at different sites. The material $Li_{1.75}MnO_3$ shows the least vacancy formation energy compared to the other materials. This alludes that creating vacancies at the 2c sites requires the least energy and therefore most desirable.

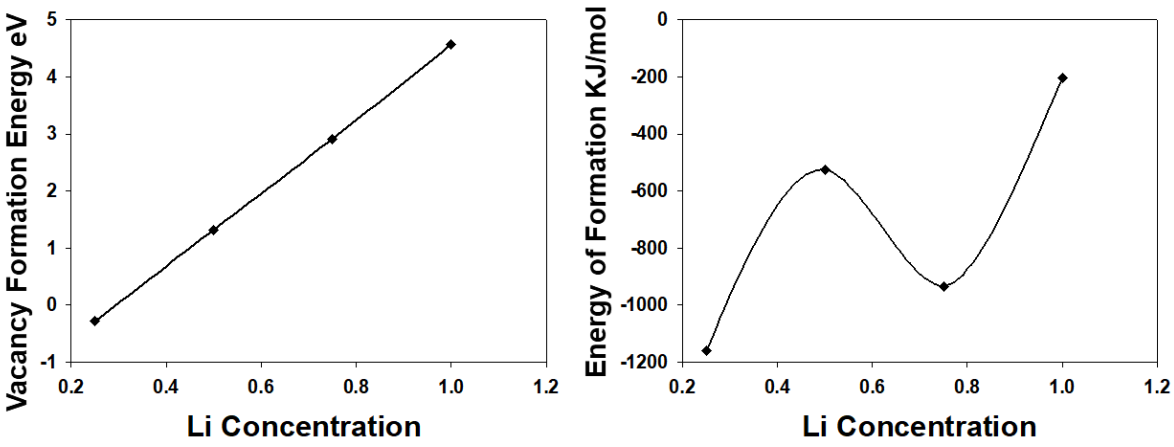

Figure 3.9. Plots for vacancy formation energy and energy of formation against the different concentrations of lithium.

3.4.2. Electronic properties of $Li_{2-x}MnO_3$

This segment introduces and analyses the computed densities of states (DOS) and the electronic band structures for $Li_{2-x}MnO_3$ (x = 0.25, 0.50, 0.75, and 1.00) structures. The density of states (DOS) pertains to the available energy levels for electrons with different numbers of states. This metric proves valuable in assessing the stability trends of structures with identical compositions, especially concerning their behaviour at the Fermi level (E_f). In all the density of states figures, the top plots depict the total DOS, while the subsequent lower plots

portray the partial DOS. The positive scale of TDOS corresponds to spin-up states, while the negative scale represents spin-down states. The total DOS offers insights into the overall electronic contribution of the entire system, whereas the partial DOS elucidates the contributions of each individual atom. The electronic band structures are graphical representations of energy plotted against wave vectors for various bands. They aid in identifying whether the material exhibits insulator, semiconductor, or conductor/metal properties by delineating the magnitude of energy band gaps around the Fermi level. An energy band gap refers to the separation between the valence band and the conduction band of electrons. The DOS and electronic band structures computations were carried out using spin-polarized local density approximation with Hubbard correction (U) value of 5 eV at 0K.

i) Density of states

Figure 3.10 (a) illustrates the partial and total density of states for $Li_{1.75}MnO_3$. Examining the partial density of states reveals that the contribution to the PDOS for Li primarily comes from the d states of the atom. Similarly, the PDOS for Mn is influenced by the d states of the atom. In contrast, the PDOS for O is significantly influenced by the p states of the atom. Analysing the total density of states indicates that Li makes a modest contribution to both the valence and conduction bands. Meanwhile, Mn contributes to both bands, with a greater emphasis on the valence band. The O atom significantly contributes to both the valence and conduction bands due to its p states. Furthermore, an electron overlap is observed at the Fermi level, resulting from the p states of the O atom. This overlap leads to a band gap of 3.03 eV. The presence of this gap suggests that the material exhibits characteristics of a half-metallic ferromagnet which means that the material exhibits metallic behaviour in one spin while displaying semiconducting or insulating properties in the other.

Figure 3.10 (b) depicts the partial and total density of states for $Li_{1.5}MnO_3$. Analysing the partial density of states reveals that the contribution of the Li atom

to the material's DOS is minimal. In contrast, the PDOS of the Mn atom is predominantly influenced by its d states. The PDOS of the O atom is primarily attributed to both its p and d states, with a greater emphasis on the p states. It is noteworthy that the Li atom makes no contribution to the total density of states (TDOS) of the material. On the other hand, the Mn atom contributes to both the valence and conduction bands of the TDOS, with a significant emphasis on the valence band. The O atom contributes substantially to both the conduction and valence bands of the TDOS. An electron overlap at the Fermi level in the TDOS is observed, stemming from both the p and d states of O and the d states of Mn. In conclusion, the material $Li_{1.5}MnO_3$ is identified as a half-metallic ferromagnet with a zero-band gap which means that the material exhibits metallic behaviour in one spin while displaying semiconducting or insulating properties in the other.

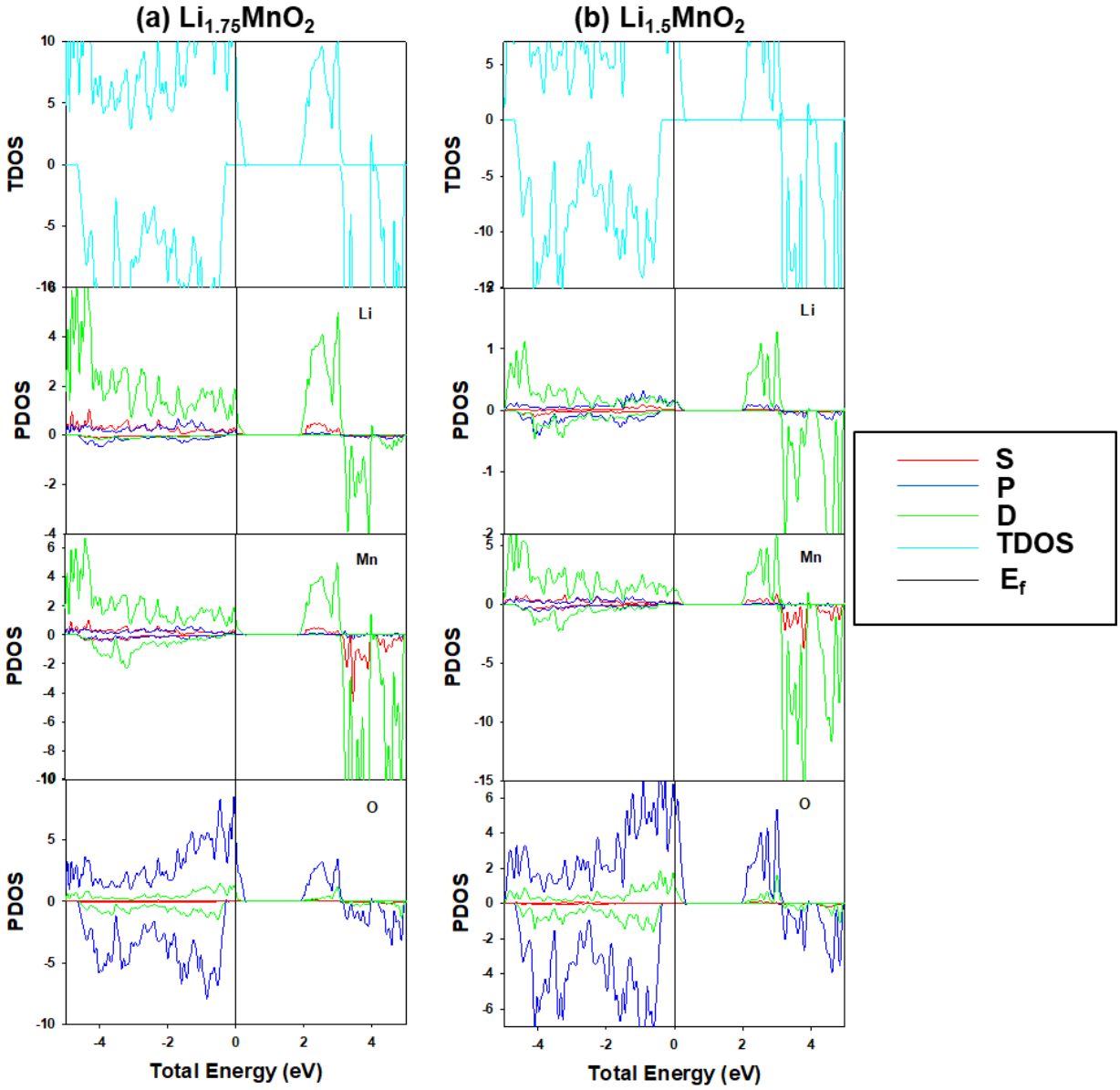

Figure 3.10. The partial and total density of states for (a) $Li_{1.75}MnO_3$ and (b) $Li_{1.5}MnO_3$ in a spin-polarized configuration.

Figure 3.11 (a) shows the partial and total density of states for $Li_{1.25}MnO_3$. Examining the partial density of states reveals that the Li atom has the least contribution to the material's DOS. In contrast, the PDOS of the Mn atom is significantly influenced by its d states. The PDOS of the O atom is primarily attributed to both p and d states, with a greater emphasis on the p states. Notably, the Li atom does not contribute to the total density of states (TDOS) of the material. On the other hand, Mn contributes to both the valence and conduction

bands of the TDOS, with a predominant influence on the valence band. The O atom contributes significantly to both the conduction and valence bands of the TDOS. An electron overlap is observed at the Fermi level of the TDOS, resulting from the contributions of both the p and d states of O and the d states of Mn. The material $Li_{1.25}MnO_3$ is identified as a half-metallic ferromagnet with a zero-band gap which means that the material exhibits metallic behaviour in one spin while displaying semiconducting or insulating properties in the other.

Figure 3.11 (b) displays the partial and total density of states for $LiMnO_3$. Analysing the partial density of states highlights that the Li atom has the least contribution to the material's DOS. Conversely, the PDOS of the Mn atom is significantly influenced by its d states. The PDOS of the O atom is primarily attributed to both p and d states, with a greater emphasis on the p states. Importantly, the Li atom makes no contribution to the total density of states (TDOS) of the material. In contrast, Mn contributes to both the valence and conduction bands of the TDOS, with a particularly pronounced effect on the valence band. The O atom contributes significantly to both the conduction and valence bands of the TDOS. An electron overlap is observed at the Fermi level of the TDOS, arising from the contributions of both the p and d states of O and the d states of Mn. The material $LiMnO_3$ is characterized as a half-metallic ferromagnet with a zero-band gap which implies that the material exhibits metallic behaviour in one spin while displaying semiconducting or insulating properties in the other.

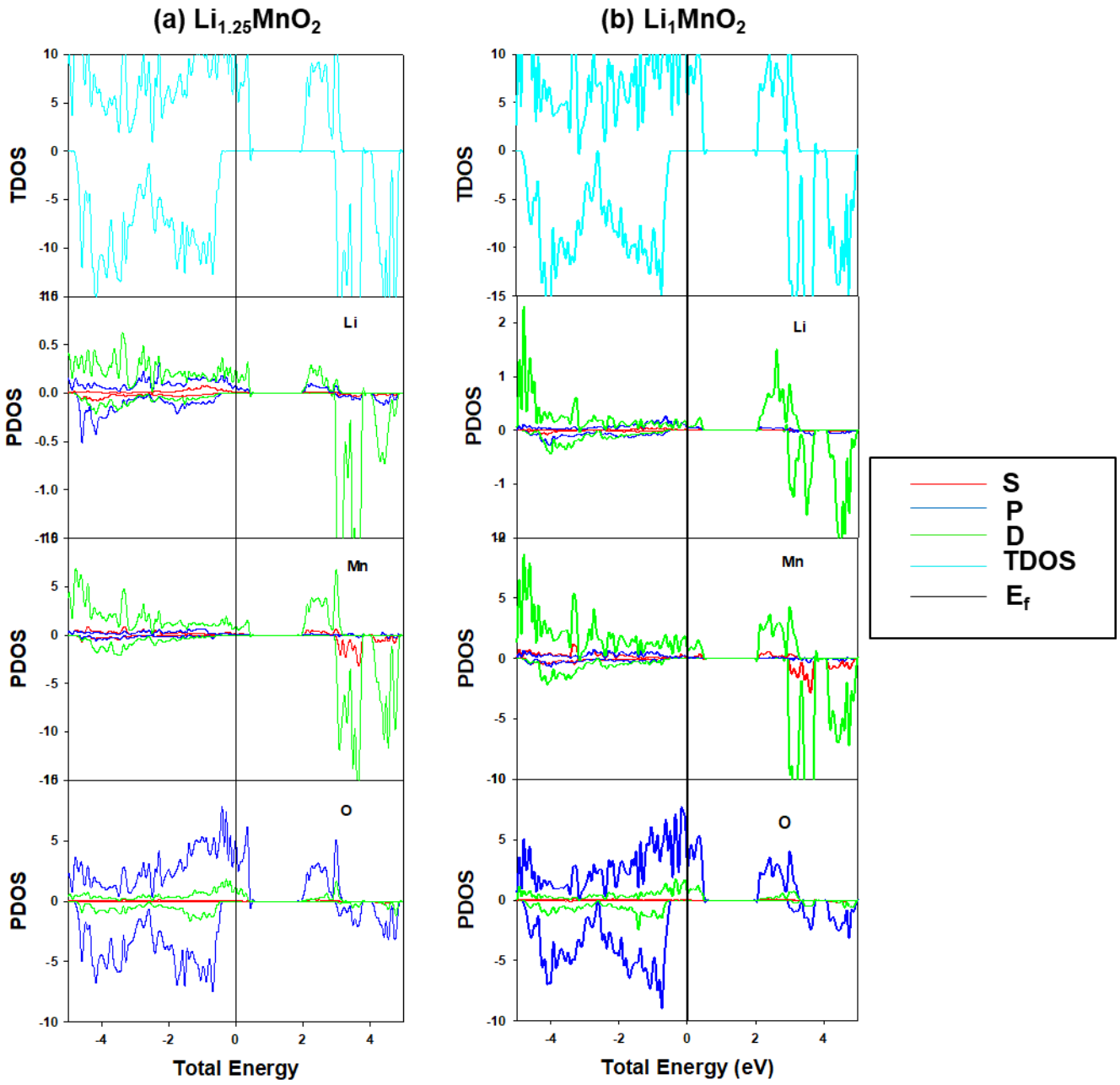

Figure 3.11. The partial and total density of states for (a) $Li_{1.25}MnO_3$ and (b) Li_1MnO_3 in a spin-polarised configuration.

ii) Electronic band structures

Figure 3.12 below illustrates the electronic band structures for (a) $Li_{1.75}MnO_3$ and (b) $Li_{1.5}MnO_3$. Examination of the electronic structure depicted in Figure 3.13 (a) reveals that the system exhibits characteristics of a half-metallic ferromagnet which means that the material exhibits metallic behaviour in one spin while

displaying semiconducting or insulating properties in the other. The bands corresponding to spin-up display metallic properties, with the Fermi energy. On the other hand, bands associated with spin-down exhibit insulating behaviour. In contrast, the minimum of the conduction band is located close to the origin (0.00 0.00 0.00), with an energy of 2.953 eV relative to the Fermi level. The direct band gap is measured at 3.030 eV. It is important to note that the Fermi energy serves as the reference point, defining the zero of the energy scale.

The analysis of the electronic structure presented in Figure 3.12 (b) indicates that the system exhibits characteristics of a half-metallic ferromagnet which means that the material exhibits metallic behaviour in one spin while displaying semiconducting or insulating properties in the other. Bands corresponding to spin-up demonstrate metallic properties, with the Fermi energy. Conversely, bands associated with spin-down display semiconducting behaviour. The maximum of the valence band is at -0.140 eV with respect to the Fermi level. In contrast, the minimum of the conduction band is with an energy of -0.450 eV concerning the Fermi level. The system features an indirect band gap of 0.000 eV. It's noteworthy that the Fermi energy serves as the zero point on the energy scale.

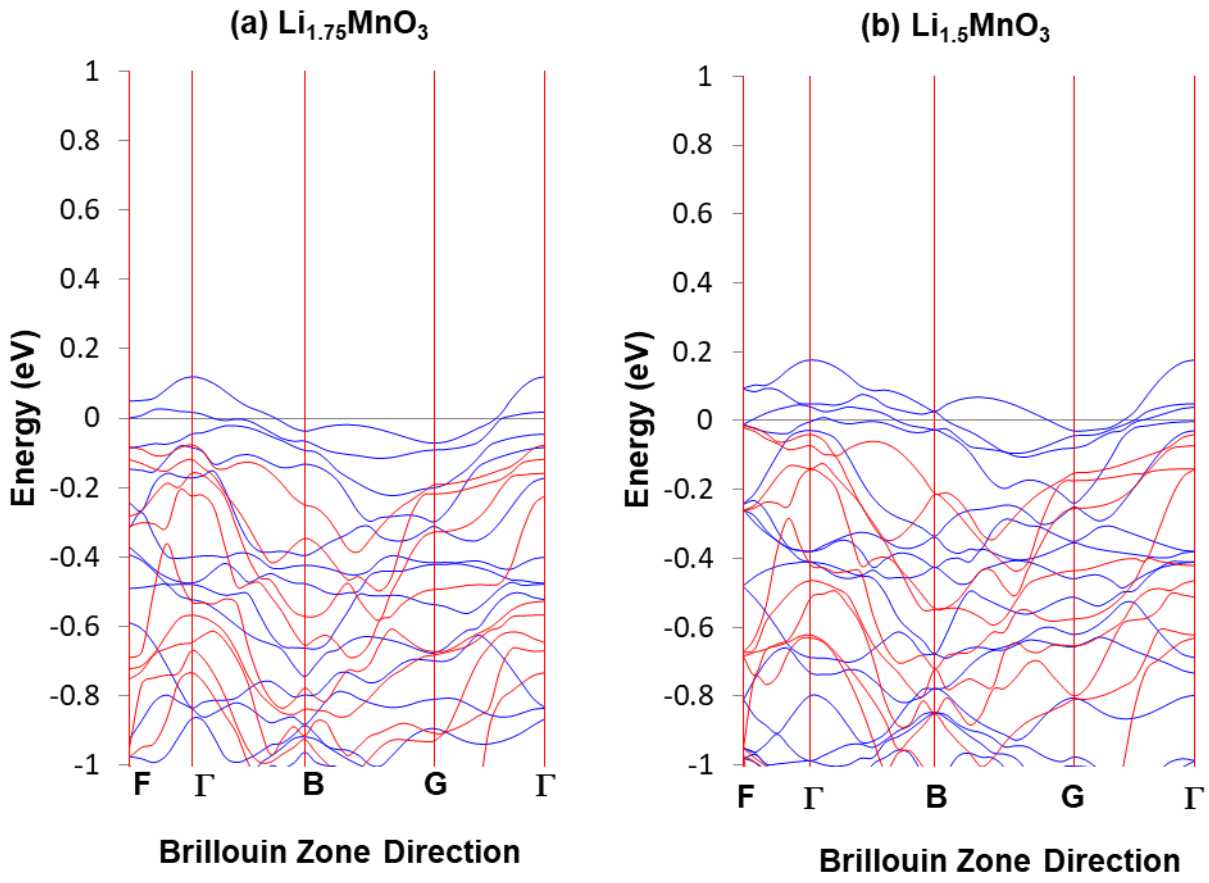

Figure 3.12. The electronic band structures for (a) $Li_{1.75}MnO_3$ and (b) $Li_{1.5}MnO_3$.

Examining the electronic structure in Figure 3.13 (a) reveals that the system displays characteristics of a half-metallic ferromagnet. Bands associated with spin-up exhibit metallic behaviour, with the Fermi energy. In contrast, bands related to spin-down demonstrate semiconducting properties. The maximum of the valence band is at -0.084 eV with respect to the Fermi level. Conversely, the minimum of the conduction band is with an energy of -0.364 eV concerning the Fermi level. The system features an indirect band gap of 0.000 eV. It is important to note that the Fermi energy serves as the zero point on the energy scale.

Examining the electronic structure presented in Figure 3.13 (b) reveals that the system is a magnetic metal. The Fermi energy is covering an energy range of (-

0.064 to 0.086) eV concerning the Fermi level. The Fermi energy is employed as the reference point on the energy scale.

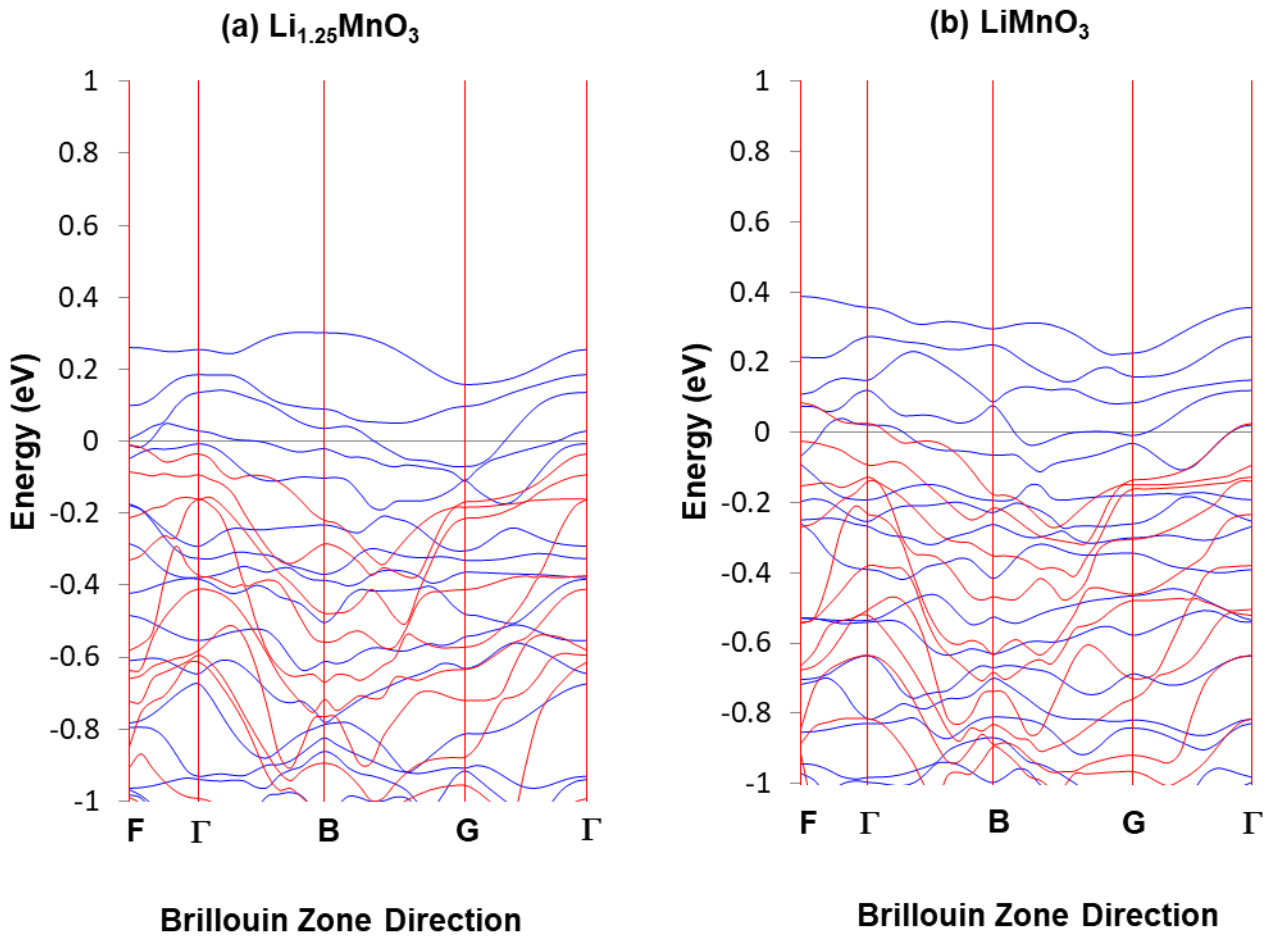

Figure 3.13. The electronic band structures for (a) $Li_{1.25}MnO_3$ and (b) $LiMnO_3$.

3.5. Voltages

Investigating voltage profiles during the delithiation process is crucial for gaining insights into the electrochemical processes that occur within lithium-ion batteries (LIBs) as they discharge. The voltage profile, representing the relationship between the cell voltage and the state of charge, provides valuable information about the redox reactions and phase transitions taking place in the electrode materials. Understanding these processes is essential for optimizing the performance and safety of LIBs. Voltage profiles offer details on the kinetics of lithium extraction from the electrode, the occurrence of side reactions, and the

stability of the electrode materials. This knowledge is vital for designing advanced electrode materials, improving the overall energy density, and addressing challenges such as capacity fading and cycle life.

In Figure 3.10 presented below, the voltage trend for the delithiated materials $L_{1.75}MnO_3$, $Li_{1.5}MnO_3$, $Li_{1.25}MnO_3$, and Li_1MnO_3 is illustrated. The voltage values were determined utilizing the equation:

$$V_{ave}(x_1 \leq x \leq x_2) = -\frac{E_{Li_{x2-x1}MnO_3} - E_{Li_{2-x1}MnO_3} - (x_2 - x_1)E_{Li}}{(x_2 - x_1)e},$$

where E represents the total energy calculated in electron volts (eV). The graph in Figure 3.14 clearly indicates that the average charging voltage rises as more lithium is removed from the system.

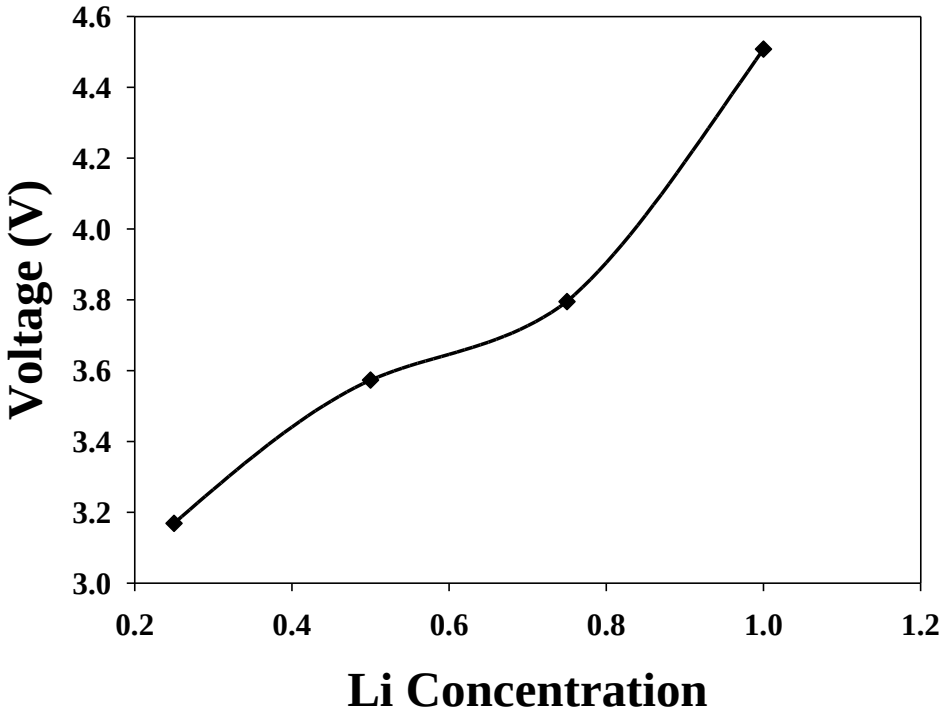

Figure 3.14. The voltages of the delithiated materials plotted against concentration.

3.6. Discussion

This section aimed to explore the structural and electronic characteristics of O2-type $Li_{0.69}MnO_2$ and Li_2MnO_3, with a primary focus on studying the delithiation process of $Li_{2-x}MnO_3$ ($0 \leq x \leq 1$) to gain a deeper understanding of the material's electrochemical behaviour. Lattice parameters provided insights into the atomic arrangements of the investigated materials, revealing the triclinic crystal structure with space group $P6_3/mm$ for the O2-type material and the monoclinic structure with space group C2/m for the O3-type material.

The density of states analysis for the O2 material indicated that the electron contribution at the Fermi level originated from the p state of oxygen and the d state of manganese. The band structure suggested a metallic character with a zero-band gap. In contrast, the density of states for the O3 material revealed a significant contribution to the Fermi level from the p states of oxygen and the d states of manganese. The band structure showed a band gap of 1.781 eV, indicating semiconductive behaviour.

The delithiated structures were optimized with the previously determined cutoff energy and k-point mesh for the parent Li_2MnO_3 material to determine their electronic properties. Analysing the properties of the delithiated materials revealed a conductivity shift in the system, transitioning from semiconductive behaviour to magnetic metal behaviour.

CHAPTER 4

MOLECULAR DYNAMICS SIMULATIONS FOR THE CORE-SHELL NANOSPHERE

This chapter discusses in detail the process of generating the Li_2MnO_3-$Li_{0.69}MnO_2$ core-shell systems and uses the DL_POLY molecular dynamics code to investigate suitable simulation conditions for the generated core-shell systems. It further captures the variation of different simulation conditions in a quest to determine at which simulation conditions the core-shell system operates effectively.

4.1. Introduction

In recent decades, substantial efforts have been invested in the search for alternative cathode materials for lithium-ion batteries, with the goal of augmenting both their energy density and safety. The core-shell architecture represents one of the more recently explored methodologies aimed at enhancing the performance of lithium-ion batteries [61]. This technique is renowned for its capacity to elevate the electrochemical efficiency of commonly employed lithium-ion batteries by amplifying conductivity, refining physical structures, and mitigating irreversible reactions between the electrode material and electrolyte [26]. While surface coating has the potential to enhance the structural and thermal stabilities of cathode materials, preventing undesirable transformations, the challenge lies in effectively enveloping the primary particles with thin coating layers. The core-shell design, however, combines the strength of layered-layered materials, providing a thicker shell for the core material [62].

Molecular dynamics (MD) simulations serve as a powerful tool for advancing lithium-ion batteries by providing atomistic insights into the intricate processes occurring within battery materials. These simulations offer a detailed understanding of structural, thermodynamic, and kinetic properties at the atomic

level, enabling researchers to unravel complex phenomena such as ion diffusion, phase transitions, and interface interactions. MD simulations play a crucial role in investigating electrolyte-electrode interfaces, optimizing the formation and evolution of the solid-electrolyte interphase (SEI), and predicting the thermal stability of battery materials. Furthermore, MD simulations contribute to the design and evaluation of nanoscale architectures, aiding in the development of advanced electrode materials with improved electrochemical performance and mechanical stability. In molecular dynamics simulations for lithium-ion batteries, radial distribution functions (RDFs) are employed to understand the arrangement of the Li-ions in the material. By examining the probability of finding a particle at a certain distance from another particle, RDFs provide insights into the local structure, coordination environment, and ordering of particles within a material. This information is crucial for understanding the structural properties of electrode materials and electrolytes in lithium-ion batteries.

Furthermore, in lithium-ion batteries, diffusion coefficients are particularly relevant for studying the mobility of lithium ions within electrode materials or electrolytes. These coefficients provide information about the ease with which ions diffuse through the crystal lattice of electrode materials or through the liquid electrolyte. Moreover, RDFs and diffusion coefficients derived from molecular dynamics simulations are valuable tools for gaining insights into the structural arrangements and dynamic behaviour of particles within materials, contributing to the design and optimization of advanced materials for lithium-ion batteries.

4.2. Simulation procedure

The Li_2MnO_3-$Li_{0.69}MnO_2$ core-shell systems were generated using the MedeA interface. Two core-shell structures with different sizes, 1434 and 435 atoms were generated using the tools embedded on the MeDeA interface. Initially, the $Li_{0.69}MnO_2$ and Li_2MnO_3 nanospheres were generated from the bulk structures. An inner hollow spherical void big enough to accommodate the Li_2MnO_3 nanoparticle was created inside the $Li_{0.69}MnO_2$ nanoparticle, and atoms of the

inner sphere were deleted. The Li_2MnO_3 nanosphere was then inserted into the hollow sphere inside the $Li_{0.69}MnO_2$ nanosphere and adjusted to the centre of the sphere. This process yielded two core-shell structures of 1434 and 435 atoms, the nanospheres had shells of diameters 30 and 20 angstroms, cores of diameters 18 and 14 angstroms, and inner sphere radii of 10 and 7.5 angstroms, respectively. The molecular dynamics were employed to generate and study two core-shell systems of varying sizes. The subsequent figures illustrate the two Li_2MnO_3-$Li_{0.69}MnO_2$ core-shell systems that will be examined in this section.

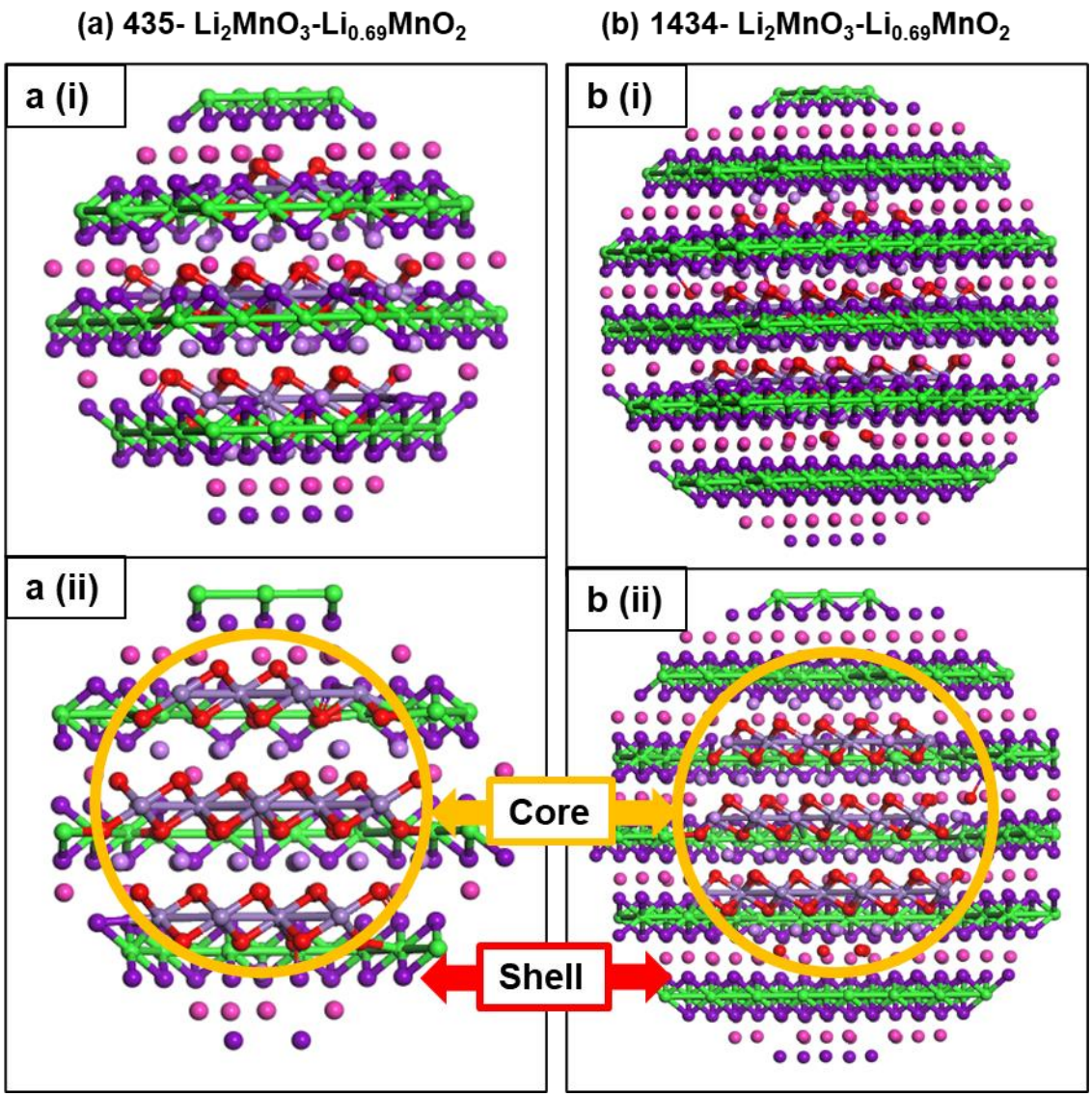

Figure 4.1. The two generated Li_2MnO_3-$Li_{0.69}MnO_2$ core-shell systems where *a (i)* represents the complete systems of 435 atoms and *a (ii)* shows a cross-section of the core-shell system and *b (i)* represents the complete system of 1434 atoms and *b (ii)* shows the cross-section of the core-shell system.

The molecular dynamics code DL_POLY version 2.20 [63] was used to run the simulations. The DL_POLY input files; CONFIG, CONTROL, and FIELD were generated using the METADISE code [64]. The molecular dynamics simulations were carried out using the NVT, NST, and NPT ensembles. The simulation conditions were constantly varied in order to eventually optimize the simulation conditions of the core-shell structures. The other crucial parameters were the time steps variation simulations as this controls the motion rate of atoms in molecular

dynamics simulations. This was followed by a constant increment in temperature until optimum variables were achieved.

4.3. Optimizing the simulation conditions for core-shell systems

This section is focused on determining the optimal operational conditions for the two Li_2MnO_3-$Li_{0.69}MnO_2$ core-shell systems. Various simulation conditions were applied to assess their behaviour. Initially, the number of steps for the systems were varied across a range of 50,000 to 150,000, observing the systems' responses under these conditions within the NST and NPT ensembles. Furthermore, the temperatures in the systems were systematically adjusted between the range of 300K to 2000K, under the NVT and NPT ensembles to explore their influence on the core-shell structures.

4.3.1. Variation of steps for 435 atoms system under NST ensemble

Figure 4.2, depicted below, illustrates the 435-atom core-shell structure under various simulation conditions with the ensemble NST. Initially, we permitted all atoms in the system to move freely during the different steps, leading to a disordered system where oxygen atoms from the core exited the system. Subsequently, by immobilizing the atoms in the core and allowing the shell atoms to move freely, a minor amount of lithium and oxygen was observed leaving the system. However, when the atoms in the shell were fixed while allowing atoms in the core to move freely, the system exhibited no loss of oxygen or lithium.

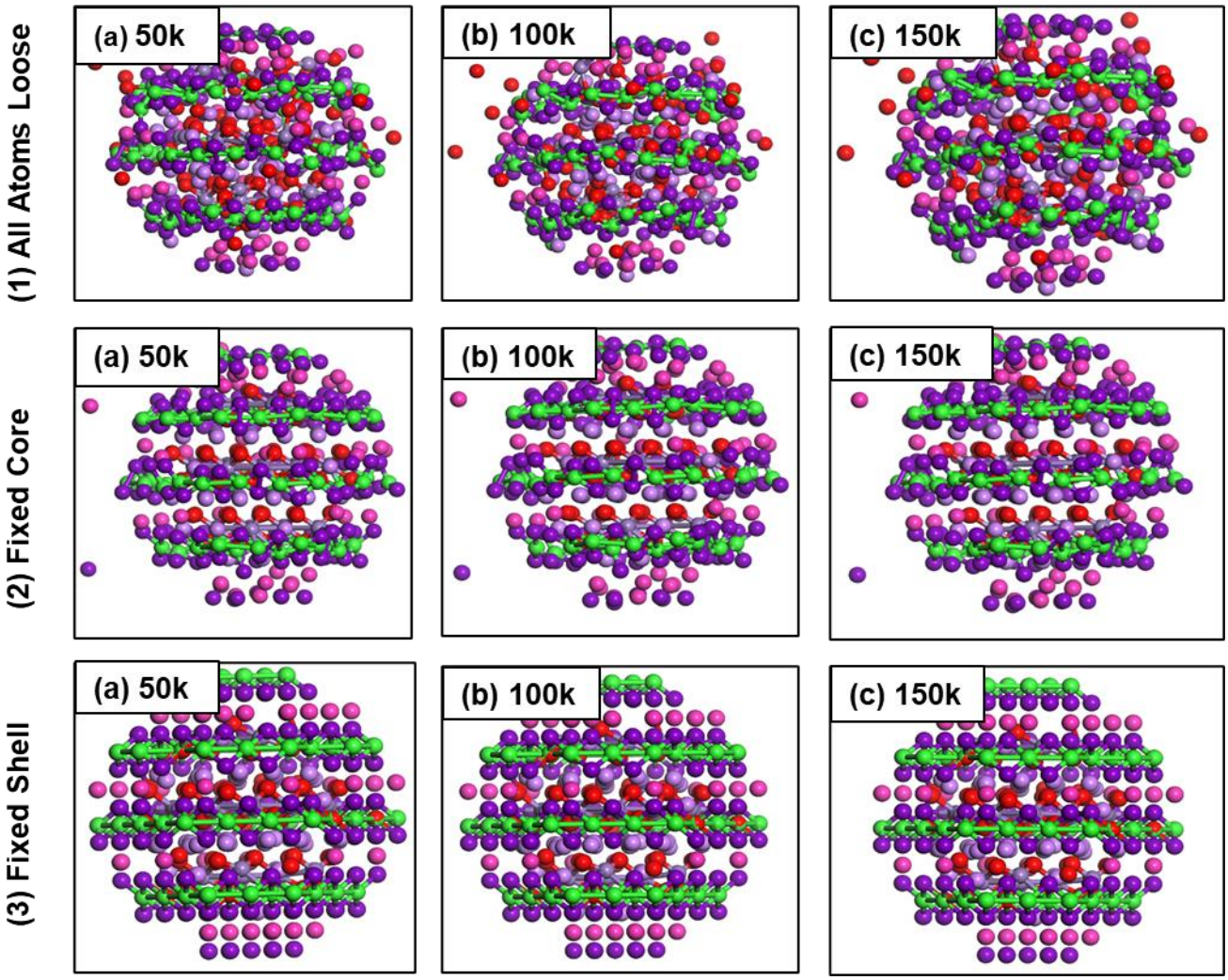

Figure 4.2. Variation of steps from 50k to 150k under NST ensemble for (1) All Atoms Loose, (2) Fixed Core, and (3) Fixed Shell.

4.3.2. Variation of steps for 435 atoms system under NPT ensemble

Figure 4.3, presented below, depicts the 435-atom core-shell structure under various simulation conditions using the NPT ensemble. Initially, we enabled unrestricted movement for all atoms in the system during the different steps, resulting in a disordered system with oxygen atoms leaving the core. Furthermore, by immobilizing the core atoms and allowing the shell atoms to move freely, the system showed no loss of oxygen or lithium. However, when we fixed the atoms in the shell and allowed the atoms in the core to move freely, a

slight amount of lithium and oxygen began leaving the system as the number of steps increased.

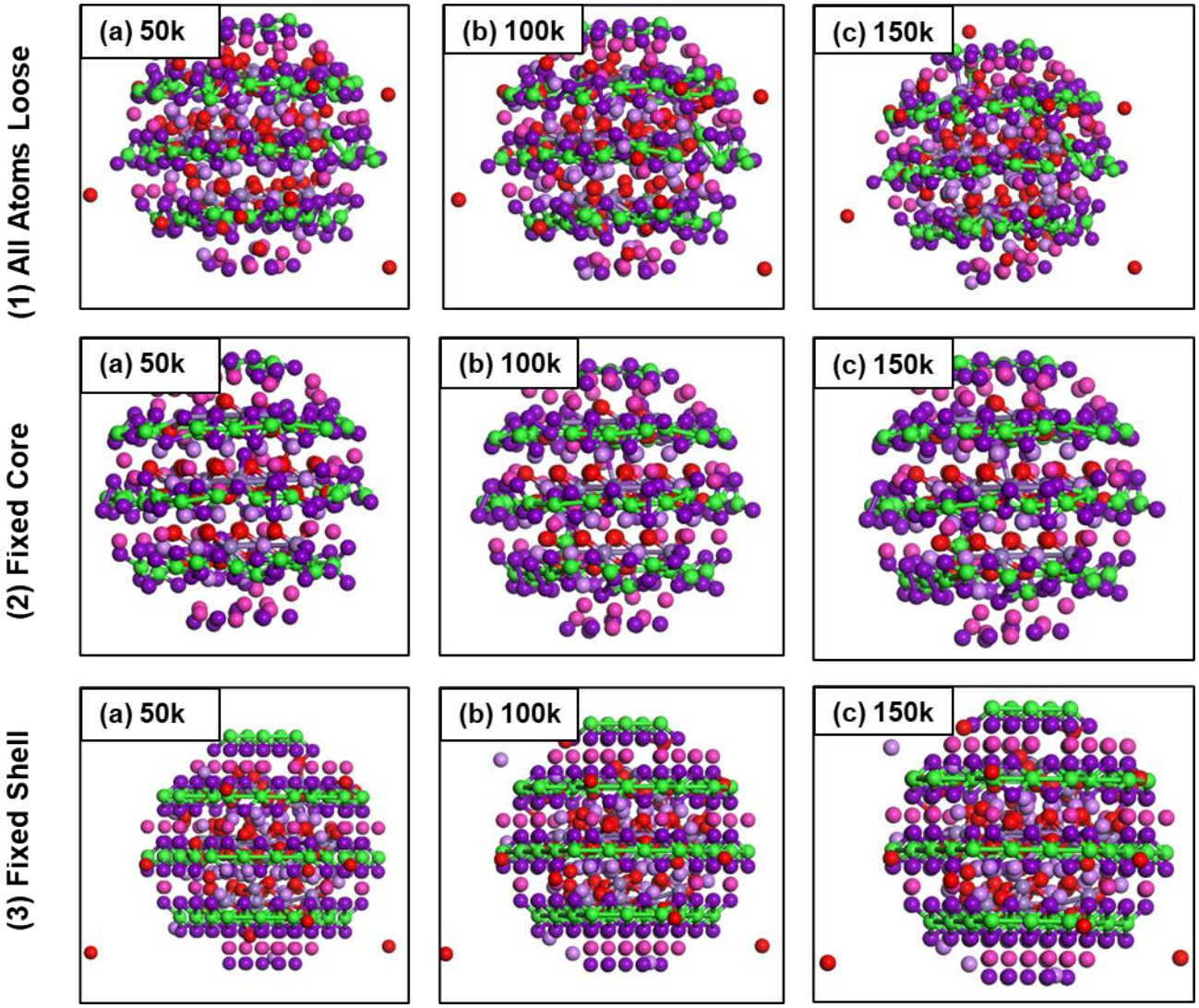

Figure 4.3. Variation of steps from 50k to 150k under NPT ensemble for (1) All Atoms Loose, (2) Fixed Core, and (3) Fixed Shell.

4.3.3. Variation of steps for 1434 atoms system under NST ensemble

The diagram in Figure 4.4 below illustrates the resulting structures for the 1434-atom Li_2MnO_3-$Li_{0.69}MnO_2$ core-shell system during variations in the number of steps under the NST ensemble. When all the atoms in the system had unrestricted movement, the system displayed disorder, accompanied by a slight

depletion of lithium and oxygen from the core. Fixing the atoms in the core while allowing those in the shell to move freely resulted in a slightly disordered shell and experienced a minor loss of oxygen. Conversely, when the shell was fixed, and atoms in the core were allowed to move freely, the core exhibited slight disorder, with a minor loss of oxygen from the core, and some oxygen from the core formed bonds with both manganese from the shell.

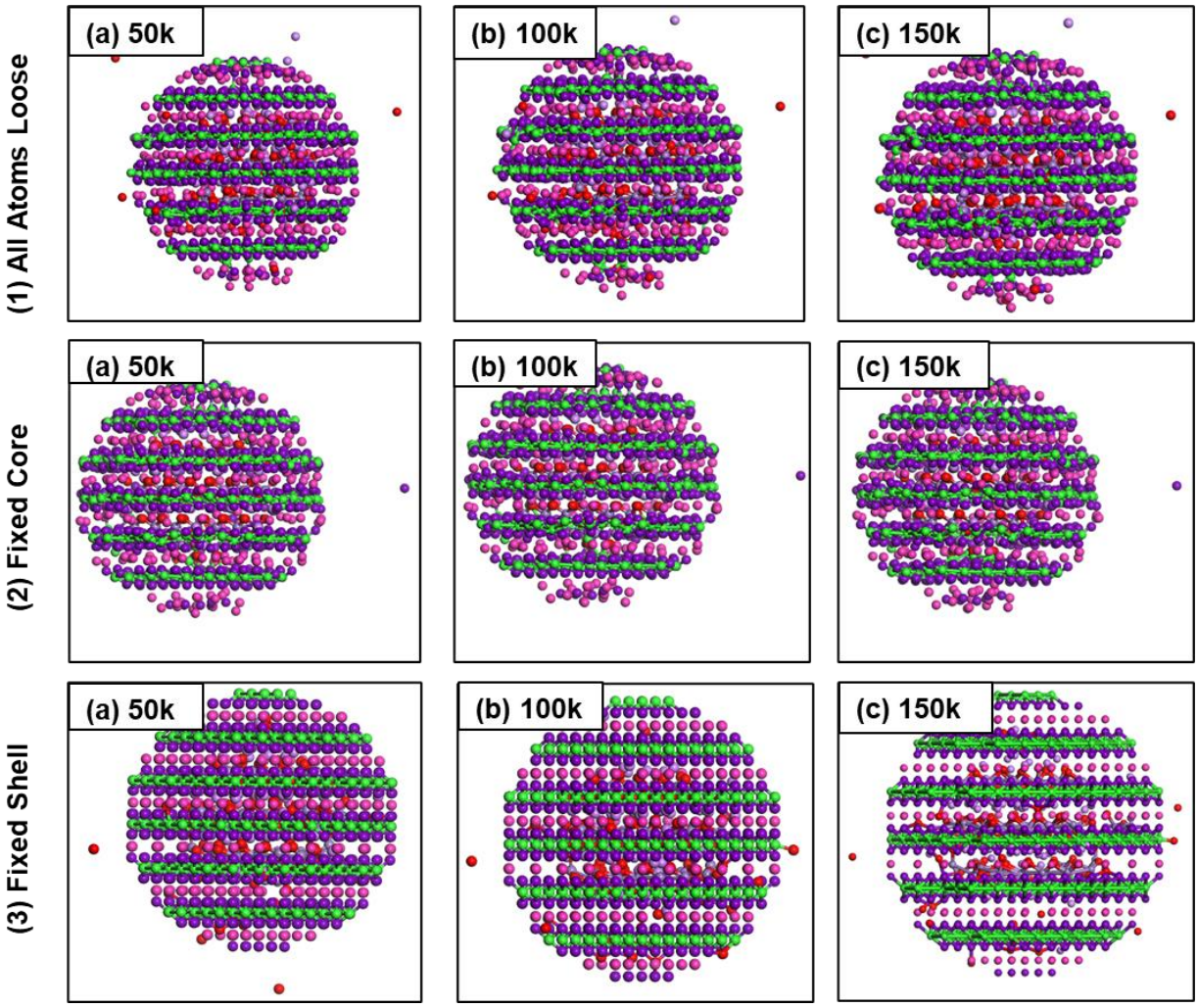

Figure 4.4. Variation of steps from 50k to 150k under NST ensemble for (1) All Atoms Loose, (2) Fixed Core, and (3) Fixed Shell.

4.3.4. Variation of steps for 1434 atoms system under NPT ensemble

Figure 4.5 below illustrates the resulting structures for the 1434-atom Li_2MnO_3-$Li_{0.69}MnO_2$ core-shell system during variations in the number of steps under the

ensemble NPT. When all the atoms in the system were permitted to move freely, the system exhibited disorder, accompanied by a slight loss of manganese and oxygen from the shell, as well as a minor loss of lithium from the core. Fixing the atoms in the core while allowing those in the shell to move freely resulted in a modest loss of manganese and oxygen. Conversely, when the shell was fixed, and atoms in the core were allowed to move freely, the core exhibited slight disorder, with a minor loss of oxygen and some oxygen from the core forming bonds with both manganese from the shell.

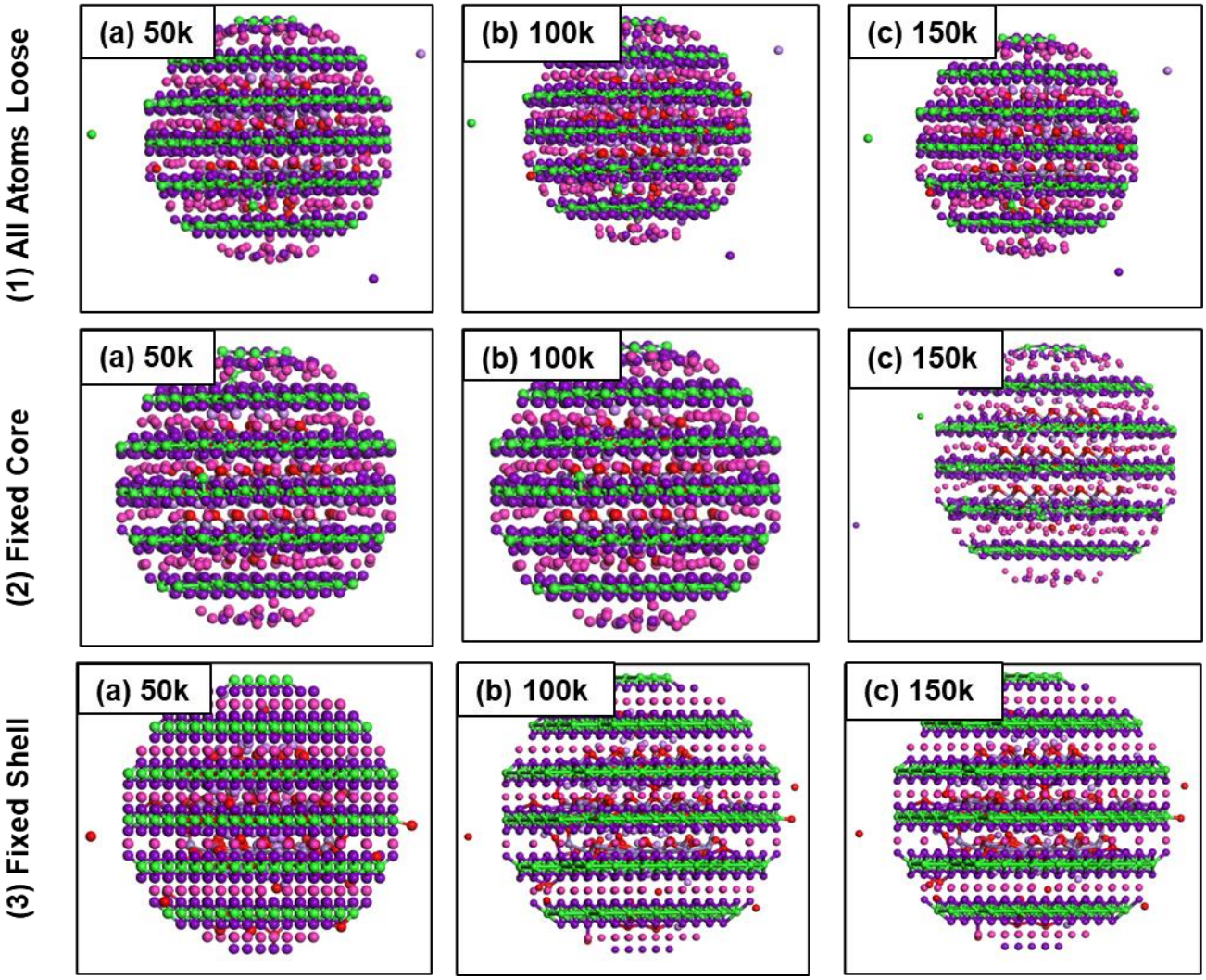

Figure 4.5. Variation of steps from 50k to 150k under NPT ensemble for (1) All Atoms Loose, (2) Fixed Core, and (3) Fixed Shell.

4.4. Temperature variation simulations

Monitoring the effects of temperature on the structural stability of the core-shell system was the next evaluation. The ability of materials to maintain thermodynamic stability under various operating conditions is crucial for ensuring the long-term reliability, efficiency, and safety of energy storage devices. Thermodynamic stability governs the reversibility of electrochemical reactions, preventing unwanted side reactions, degradation, and capacity fading during the charge-discharge cycles of batteries [65].

4.4.1. Temperature variation calculations for the 1434-atom system under the NVT ensemble

i) Structural snapshots

Figure 4.6 below illustrates the Li_2MnO_3-$Li_{0.69}MnO_2$ core-shell system consisting of 1434 atoms under different temperature conditions. The atoms within the system were allowed to move freely as the temperature increased progressively from 300 K to 2000 K. Initially, at room temperature (300 K), the system exhibited slight disorder, with a minor loss in lithium from the shell and a slight loss of oxygen from the core. As the temperature rose to 600 K and 900 K, the disorder increased, accompanied by further loss of lithium from the shell and oxygen and manganese from the core. At 1200 K, the system reached its maximum disorder, experiencing significant losses in lithium from the shell and manganese and oxygen from the core. Surprisingly, at 1500 K, the system exhibited a trend towards order, with the least overall loss of atoms. However, as the temperature continued to rise to 2000 K, the system once again became disordered, with an increasing number of atoms leaving the system.

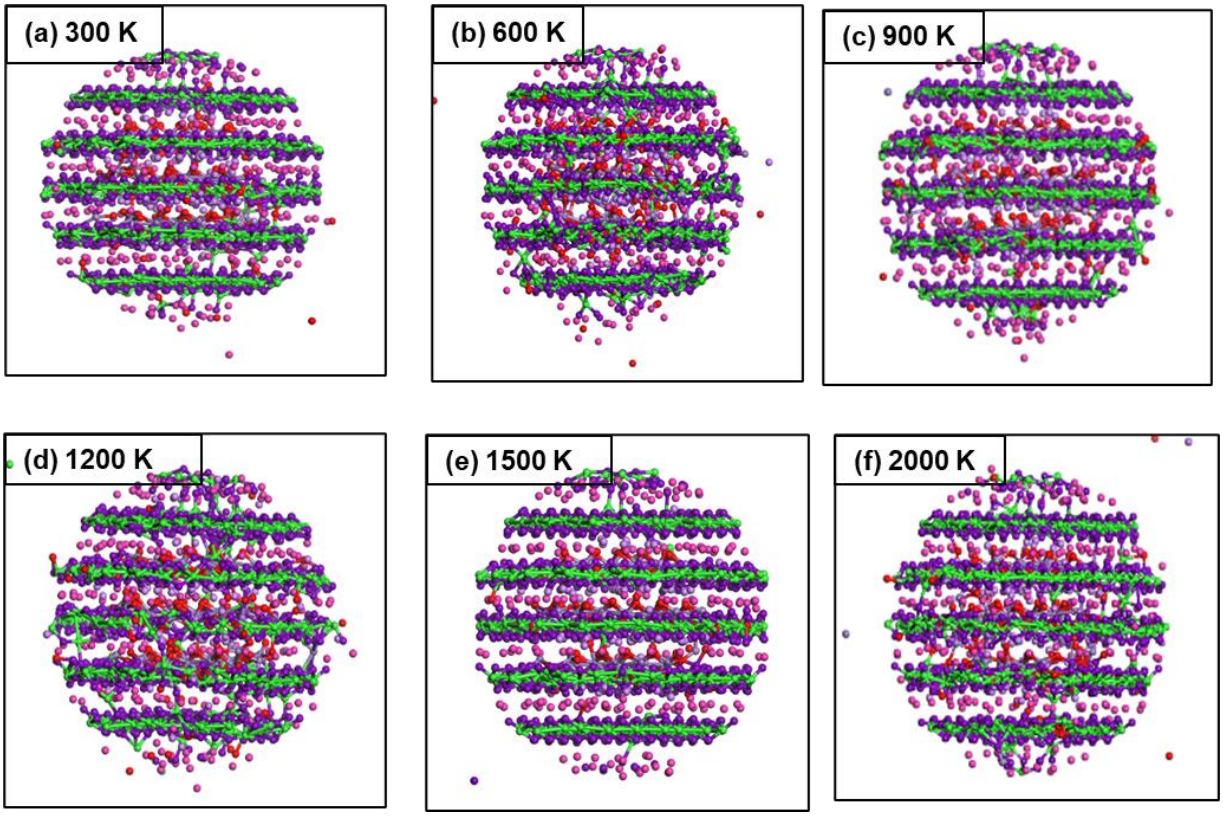

Figure 4.6. The 1434 atoms core-shell configuration at different temperatures (a) 300 K, (b) 600 K, (c) 900 K, (d) 1200 K, (e) 1500 K, and (f) 2000 K under the NVT ensemble.

ii) Radial distribution functions

In this section, the radial distribution function graphs assist with monitoring the ordering/disordering of atoms in both the core and shell components of the system. Here, particular interest is on the manganese and oxygen coordination as this governs the channels through which lithium diffuses and their thermodynamic stability is crucial. The radial distribution plots in Figure 4.7 depict manganese-oxygen interactions for the core (blue) and shell (red) at temperatures of 300 K, 600 K, 900 K, 1200 K, 1500 K, and 2000 K. At 300 K and 600 K, the radial distribution function displayed distinct peaks that demonstrate sharpness. The peaks began to flatten by 900 K implying that there may be a phase transformation taking place. However, at 1200 K and 1500 K, the peaks sharpened, resembling the radial distribution function peaks observed in a crystalline structure ordering of Mn and O atoms within the structure.

Nevertheless, the peaks resumed flattening at 2000 K, this is above the amorphisation temperature that was observed for Li_2MnO_3 in previous studies [66]. The radial distribution plots also revealed that the bonding length between manganese and oxygen was very close to 2 Å for both the core and shell which is comparable to the bond length of 1.19 Å reported by Zhang and colleagues [67].

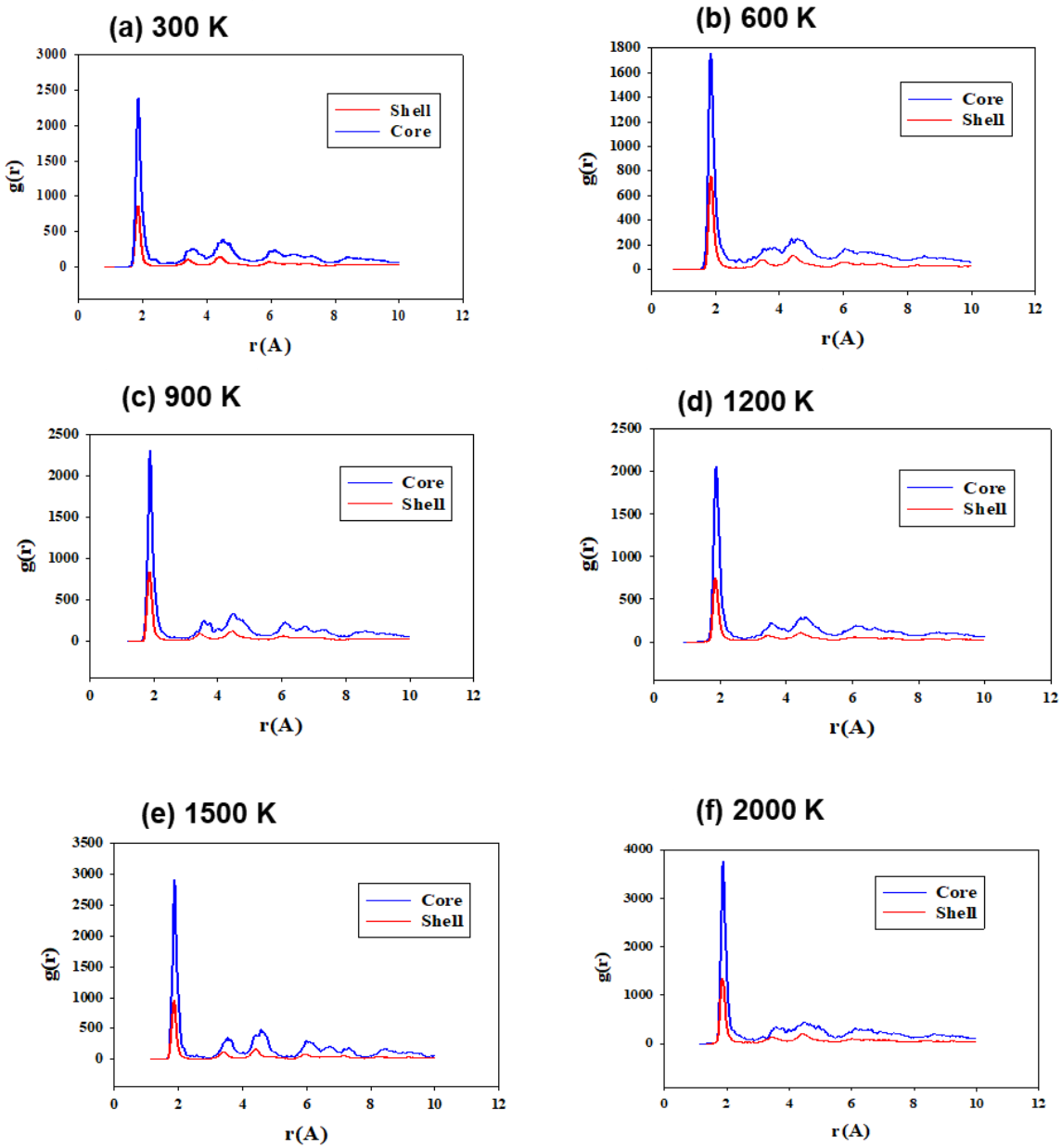

Figure 4.7. Radial distribution plots for Mn-O interactions in the core and the shell at temperatures of (a) 300 K, (b) 600 K, (c) 900 K, (d) 1200 K, (e) 1500 K, and (f) 2000 K under the NVT ensemble.

iii) Lithium diffusion coefficients

The diffusion rate of lithium from both the core and shell is illustrated in Figure 4.8 below at various temperatures. At room temperature (300 K), there is a gradual increase in the lithium diffusion rate in both the core and shell, followed by a slow decrease at 600 K and 900 K. The system exhibited its highest lithium diffusion at both the core and shell at 1200 K. However, at 1500 K, the diffusion rate decreased to a point where it became equal for both the core and shell. From the temperature 2000 K onward, there was a gradual increase in the lithium diffusion rate. The lower diffusion rates at this temperature may suggest a potential phase transformation.

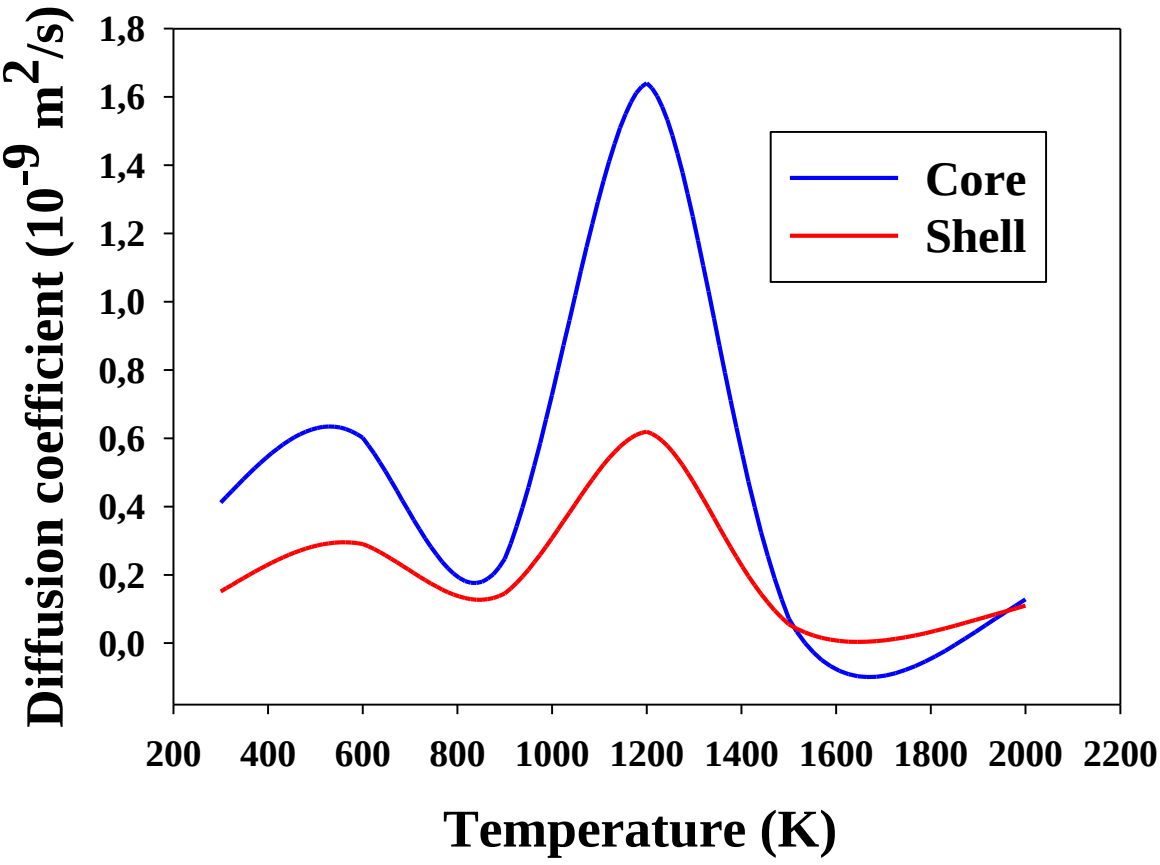

Figure 4.8: Lithium diffusion rate plots for the core and shell at different temperatures.

4.4.2. Temperature variation calculations for the 1434-atom system under the NPT ensemble.

i) Structural snapshots

The diagram in Figure 4.9 displays the core-shell system comprising 1434 atoms of Li_2MnO_3-$Li_{0.69}MnO_2$ under varying temperatures. The atoms within the system were allowed to move freely as the temperature gradually increased from 300 K to 1500K. At room temperature (300 K) and 600 K, the system exhibited slight disorder, characterized by a progressive loss of lithium from the shell and oxygen from the core. The highest level of disorder occurred at 900 K, with significant losses of lithium from the shell and manganese and oxygen from the core. At 1200 K, the system remained disordered, with a slightly reduced loss of lithium from the shell and minor losses of oxygen and manganese from the core. However, at 1500 K, an observation was made that the system started to regain order, experiencing an overall reduction in atom loss.

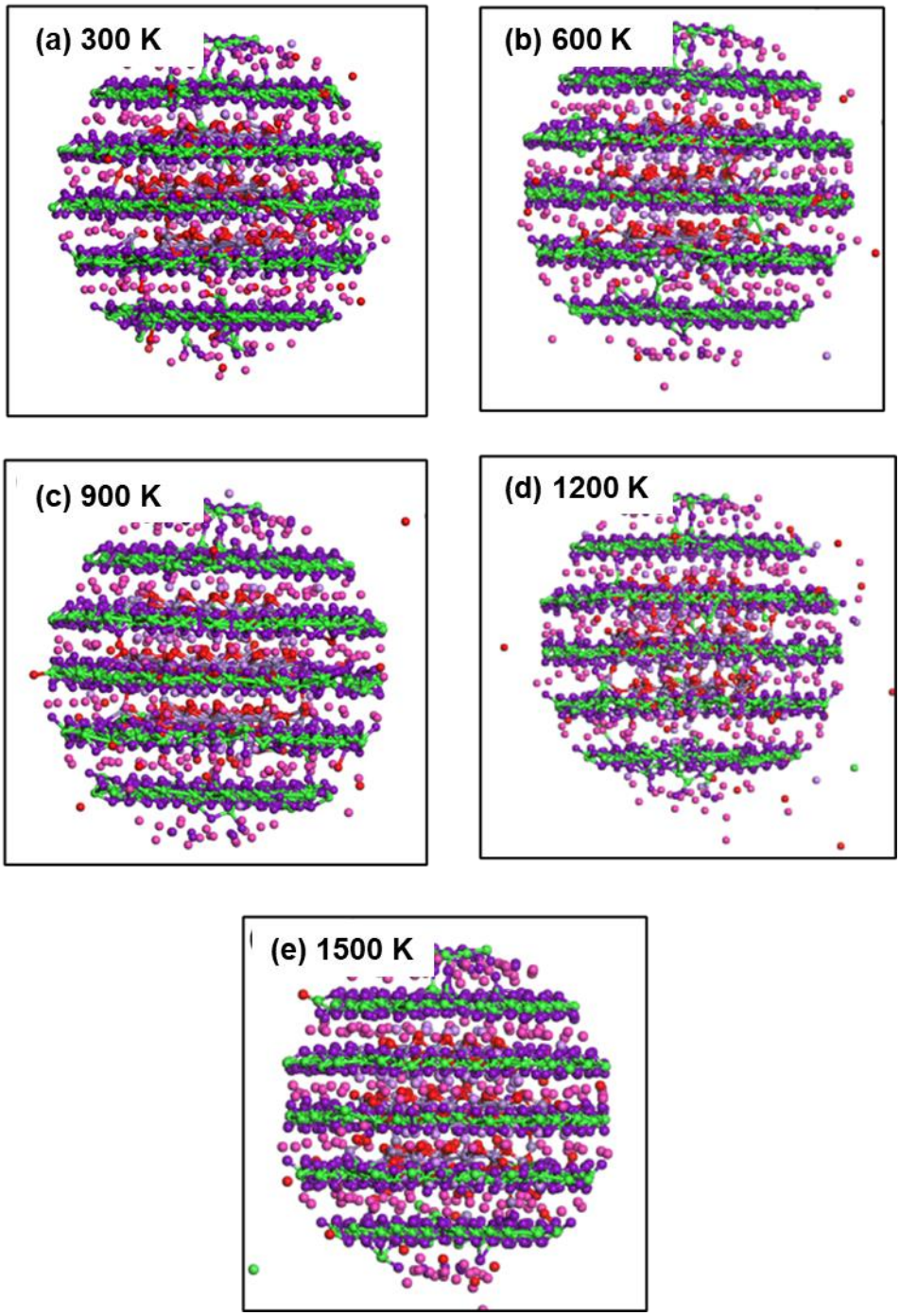

Figure 4.9. The 1434 atoms core-shell configuration at different temperatures (a) 300 K, (b) 600 K, (c) 900 K, (d) 1200 K, and (e) 1500 K under the NPT ensemble.

ii) Radial distribution functions

The radial distribution plots depicted in Figure 4.10 showcase manganese-oxygen interactions at temperatures of 300 K, 600 K, 900 K, 1200 K, and 1500

K. Following 150,000 steps at 300 K and 600 K, the radial distribution function exhibited gentle peaks that began to sharpen at 900 K. However, these peaks started to flatten once again at 1200 K. Additionally, at 1500 K, the peaks resumed sharpening, resembling the radial distribution function peaks found in a crystalline structure. The radial distribution plots also indicated that the bonding length between manganese and oxygen was very close to 2 Å for both the core and shell.

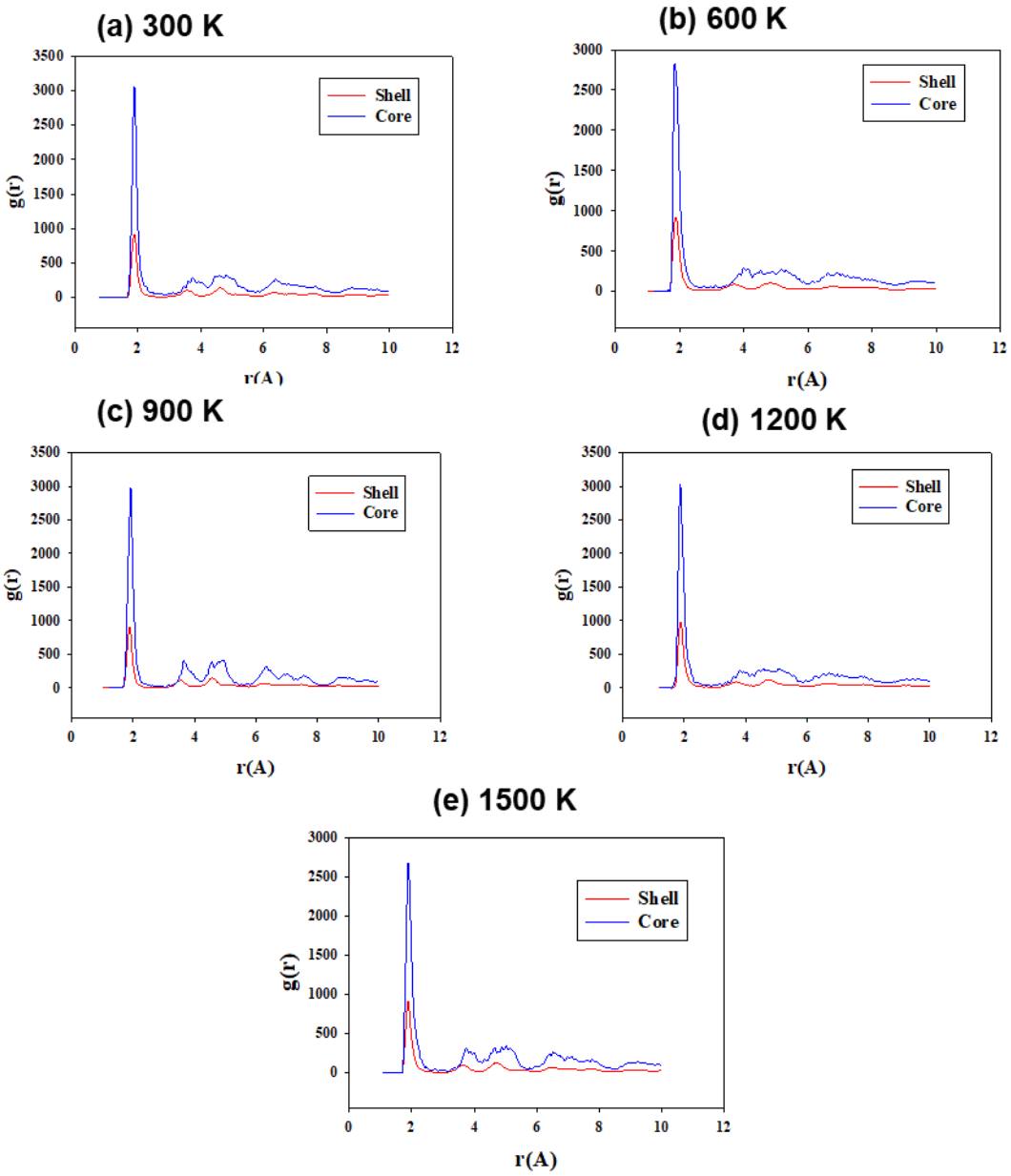

Figure 4.10. Radial distribution plots for Mn-O interactions in the core and the shell at temperature (a) 300 K, (b) 600 K, (c) 900 K, (d) 1200 K, and (e) 1500 K under the NPT ensemble.

iii) Lithium diffusion coefficients

Figure 4.11 above illustrates the lithium diffusion rate from both the core and shell at various temperatures. At room temperature (300 K) and 600 K, there is a gradual increase in the lithium diffusion rate in both the core and shell. The system reached its peak lithium diffusion rate at 900 K, observed in both the core

and shell. However, at 1500 K, the lithium diffusion rate sharply decreased for both the core and shell of the system. The reduced rates of lithium diffusion at 1500 K may suggest a potential phase transformation.

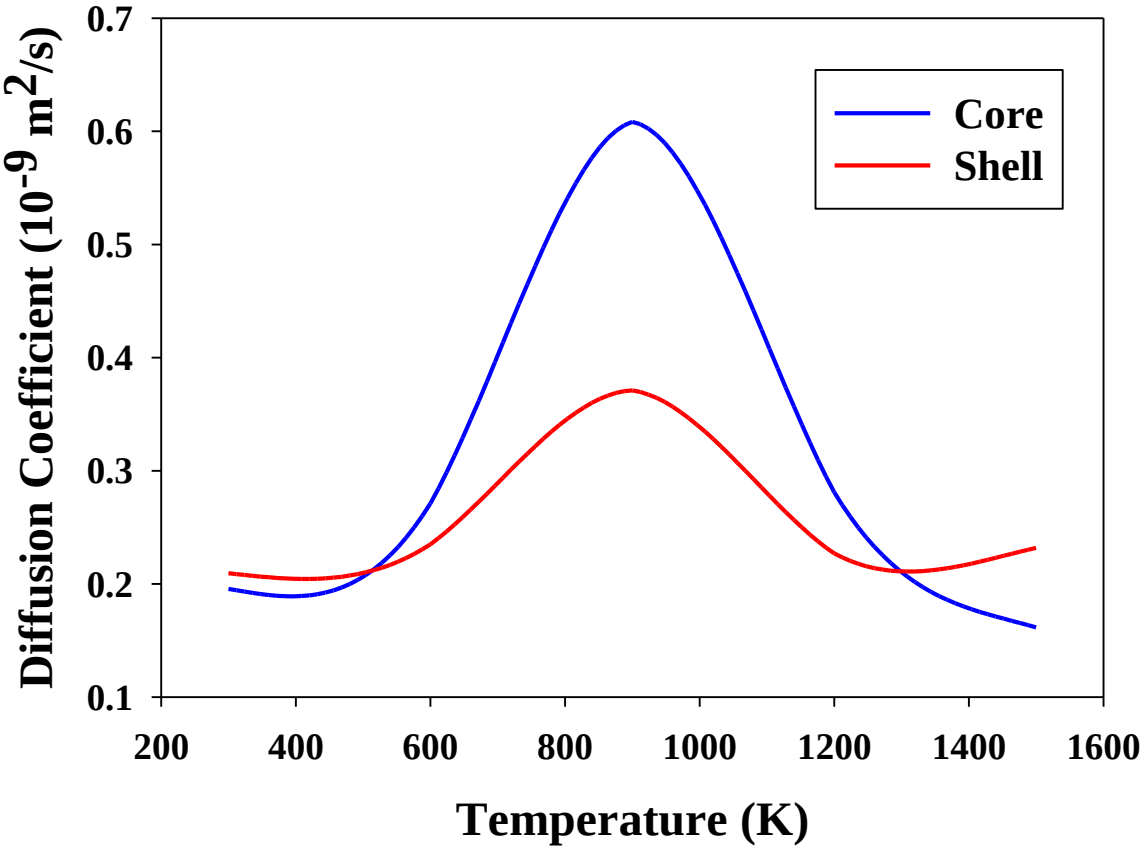

Figure 4.11. Lithium diffusion rate plots for the core and shell at different temperatures under the NPT ensemble.

4.5. Discussion

In this section, the primary goal was to optimise the simulation conditions of the created core-shell systems. Two core-shell systems, generated using the build tool within the MeDeA interface and featuring O2-type $Li_{0.69}MnO_2$ and O3-type Li_2MnO_3 materials, were examined. The number of steps varied from 50,000 to 150,000 in increments of 50,000. As the steps progressed, the core-shell systems exhibited increasing disorder. Beyond 150,000 steps, a significant disorder was observed, with atoms escaping from the systems. A time step of 0.001 was

selected, as it resulted in less disorder compared to incremental increases. This choice of 150,000 steps and a time step of 0.001 set the foundation for further temperature simulations on the 1434-atom core-shell system to explore the temperature effects on the system.

The selection of the 1434-core-shell system for temperature variation simulations was based on its superior performance compared to a smaller system. Temperature variation simulations were conducted in the NVT ensemble with temperatures ranging from 300 K to 2000 K and in the NPT ensemble with temperatures from 300 K to 1500 K.

Under NVT heating, the system exhibited increasing disorder, with lithium from the shell and atoms leaving the system at different temperatures. The temperature of 1200 K resulted in the highest disorder, with a higher diffusivity rate in lithium in both the shell and core. Radial distribution functions also indicated the least sharp peak at this temperature. However, at 1500 K, the system resembled a crystalline structure similar to that at room temperature, suggesting a potential phase transition. The RDF at 1500 K displayed sharper peaks, akin to those at room temperature, accompanied by a significant drop in lithium diffusivity for both the core and shell.

Temperature simulations under the NPT ensemble revealed the highest disorder in the system, with the greatest loss of lithium, oxygen, and manganese occurring at 900 K. Order was restored at 1500 K. The RDF at 900 K exhibited the system's sharpest peak, which flattened at 1200 K and sharpened again at 1500 K. At 900 K, the highest diffusivity rate in lithium was observed, rapidly dropping at 1500 K.

CHAPTER 5

CONCLUSIONS AND RECOMMENDATIONS

5.1. Conclusions

The rapid development of electric vehicles and large-scale renewable energy storage technology has heightened the existing need for cost-effective, high-energy-density, and high-power-density lithium-ion batteries (LIBs). Recently, there has been a particular focus on layered transition metal oxide, capable of accommodating more than one lithium unit per molecule, as a crucial component in improved cathode materials. Notably, layered Li_2MnO_3, a key element in Li-excess materials, exhibits a specific capacity reaching an ideal 459 $mAhg^{-1}$ with a distinctive first charge plateau of 4.5 V, making it a highly promising electrode material in LIBs. However, during the charging and discharging processes, structural transformations occur in Li_2MnO_3 due to the migration of the transition metal from the electrode to the electrolyte.

In efforts to enhance electrochemical performance, cathode surface modification through a coating technique has gained widespread use. The objective is to establish a core-shell system by coating Li_2MnO_3 with a stable material possessing high ionic conductivity, facilitating uninterrupted movement of Li^+ during battery operation. Before getting into the coating aspect, it is imperative to comprehend the electrochemical performance of the material without coating. This study looks into the structural and electronic properties of delithiated $Li_{2-x}MnO_3$ ($0 \leq x \leq 1$) using density functional theory. Additionally, core-shell systems are generated to serve as electrode materials, and the molecular dynamics code DL_POLY is employed to optimize the simulation conditions for these systems.

The manual delithiation process of Li_2MnO_3 was executed using BIOVIA Material Studio. Density functional theory, implemented in the Vienna Ab-initio Simulation Package (VASP), was utilized to optimize the delithiated structures, and the

CASTEP code was employed to optimize $Li_{0.69}MnO_2$. The electronic properties of the materials were calculated to elucidate their conductivity during the charging process. Analysis of electronic structures involved the density of state plots and electronic band structures.

The density of states of the O2-type $Li_{0.69}MnO_2$ suggested that the electron contribution at the fermi level was from the p states of the oxygen atom and the d states of the manganese atom. The electronic band structure indicated a zero-band gap at the fermi level, signifying metallic behaviour, making it an ideal coating material for O3-type Li_2MnO_3. Conversely, the density of states of the O3-type Li_2MnO_3 bulk structure indicated semiconductor behaviour with no electron overlap at the fermi level. The electronic band structure showed a band gap of 1.781 eV at the fermi level, confirming semiconductive properties. Delithiation shifted the material from semiconductive to magnetic metal behaviour, with $Li_{1.75}MnO_3$ exhibiting the least vacancy formation energy.

Two core-shell systems of different sizes were generated, and DL_POLY simulations were performed to optimize the steps and timesteps. The larger system demonstrated superior performance compared to the smaller one, leading to its selection for temperature simulations under NVT and NPT ensembles. Under NVT, the system experienced the highest atom loss from the core and shell at 1200 K, regaining its crystalline form at 1500 K, possibly due to a phase transformation. Lithium diffusivity peaked at 1200 K and dropped rapidly at 1500 K. Under NPT, the system experienced its highest atom loss at 900 K, regaining order at 1500 K. Lithium diffusivity was highest at 900 K and decreased at 1500 K.

5.2. Recommendations

In forthcoming research, the investigation will concentrate on the delithiation process of Li_2MnO_3 supercells and explore their electrochemical performance. Given the findings indicating superior performance in the 1434-atom system

compared to the 435-atom system, the delithiated structures of $Li_{2-x}MnO_3$ supercells will be employed to create larger core-shell systems. DL_POLY simulations will be conducted, encompassing the optimization of operational conditions for the systems, as well as the exploration of Amorphization and Recrystallisation phenomena.

REFERENCES

[1] X. He, S. Sun, L. W. Leong, P. T. Cong, A. Abu-Rumman and K. Halteh, “Does clean energy and technological innovation mmatter for economic growth? An Asian countries perspective,” *Economic Anallysis and Policy,* vol. 78, pp. 1195-1208, 2023.

[2] T. T. Salunkhe, A. N. Kadam, J. Hur and I. T. Kim, “Green and sustainably designed intercalation-type anodes for emerging lithium dual-ion batteries with high energy density,” *Journal of Energy Chemistry,* vol. 80, pp. 466-478, 2023.

[3] M. A. Naeem, M. Appiah, J. Taden, R. Amoasi and B. A. Gyamfi, “Transitioning to clean energy: Assessing the impact of renewable energy, bio-capacity andaccess to clean fuel on carbon emissions in OECD economies,” *Energy Economics,* vol. 127, p. 107091, 2018.

[4] K. Raut, A. Shendge, J. Chaudhari, R. Lamba and N. F. Alshammari, “Modeling and simulation of photovoltaic powered battery-supercapacitor hybrid energy storage system for electric vehicles,” *Journal of Energy Storage,* vol. 82, p. 110324, 2024.

[5] X. Li, L. Pan and J. Zhang, “Development status evaluation and path analysis of regional clean energy power generation in China,” *Energy Strategy Reviews.*

[6] J. Mitali, S. Dhinakaran and A. A. Mohamad, “Energy storage systems: a review,” *Energy Storage and Saving,* vol. 1, pp. 166-216, 22.

[7] W. Liu, T. Placke and K. T. Chau, “Overview of batteries and battery management for electric vehicles,” *Energy Reports,* vol. 8, pp. 4058-4084, 2022.

[8] R. Veena, J. A. Dinesh, S. Raman, P. Panigrahi and N. G. Subramaniam, “Li and Mn-rich $Li_4Mn_5O_{12}$–Li_2MnO_3 composite cathode for next generation lithium-ion batteries,” *Journal of Energy Storage,* vol. 24, p. 100754, 2019.

[9] Y. Chen, S. Liu, Z. Bi, Z. Li, F. Zhou, R. Shi and T. Mu, “Reviewing electrochemical stability of ionic liquids-/deep eutectic solvents-based

electrolytes in lithium-ion, lithium-metal and post-lithium-ion batteries for green and safe energy," *Green Energy & Environment,* pp. 1-26, 2023.

[10] Z. Xu, N. Xie and K. Li, "Remaining useful life prediction for lithium-ion batteries with an improved grey particle filter model," *Journal of Energy Storage,* vol. 78, p. 110081, 2024.

[11] S. S. Rangarajan, S. P. Sunddararaj, A. Sudhakar, C. K. Shiva, U. Subramaniam, E. R. Collins and T. Senjyu, "Lithium-ion batteries- the crux of electric vehicles with opportunities and challenges," *Clean Technologies,* vol. 4, pp. 908-930, 2022.

[12] J. Li, J. Camardese, R. Shunmugasundaram, S. Glazier, Z. Lu and J. R. Dahn, "Synthesis and characterization of the lithium-rich core-shell cathodes with low irreversible capacity and mitigated voltage fade," *Chemistry of Materials,* vol. 27, p. 3366–3377, 2015.

[13] J.-K. Nah, S. Kim, H. Kim, W. Choi, W. Chong, D. Byung, B.-W. Cho and K. Y. Chung, "Mechanochemical synthesis of Li_2MnO_3 Shell/$LiMO_2$ (M=Ni, Co, Mn) core-structured nanocomposites for lithium-ion batteries," *Scientific Reports,* vol. 4, pp. 1-9, 2014.

[14] Q. Zhang, Q.-F. Gu, Y. Li, H.-N. Fan, W.-B. Luo, H.-K. Liu and S.-X. Dou, "Surface stabilization of O3-type layered oxide cathode to protect the anode of sodium ion batteries for superior lifespan," *iScience,* vol. 19, pp. 244-254, 2019.

[15] M. P. Bondarde, R. Jain, J. S. Sohn, K. D. Lokhande, M. A. Bhakare, P. S. Dhumal and S. Some, "Carbon-based anode materials for lithium-ion batteries," in *Lithium Sulfur Batteries*, 2022, pp. 521-545.

[16] M. Kamran and M. R. Fazal, "Fundamentals of renewable energy systems," in *Renewable Energy Conversion Systems*, 2021, pp. 1-19.

[17] J.-Y. Hwang, S.-T. Myung, J. U. Choi, C. S. Yoon, H. Yashiro and Y.-K. Sun, "Resolving the degradation pathways of the O3-type layered oxide cathode surface through the nano-scale aluminum oxide coating for high-energy density sodium-ion batteries," *Journal of Materials Chemistry A,* vol. 5, pp. 23671-23680, 2017.

[18] Y. Liu, X. Fang, A. Zhang, C. Shen, Q. Liu, H. A. Enaya and C. Zhou, “Layered P2-$Na_{2/3}[Ni_{1/3}Mn_{2/3}]O_2$ as high-voltage cathode for sodium-ion batteries: The capacity decay mechanism and Al_2O_3 surface modification,” *Nano Energy,* vol. 27, pp. 27-34, 2016.

[19] S. F. Amalraj, D. Sharon, M. Talianker, C. M. Julien, L. Burlaka, R. Lavi, E. Zhecheva, B. Markovsky, E. Zinigrad, D. Kovacheva, R. Stoyanova and D. Aurbach, “Study of the nanosized Li_2MnO_3: Electrochemical behavior, structure, magnetic properties, and vibrational modes,” *Electrochemica Acta,* vol. 97, pp. 259-270, 2013.

[20] C. O. Ehi-Eromosele, S. O. Ajayi and C. N. Onwucha, “Optimizing the electrochemical performance of Li_2MnO_3 cathode materials for Li-ion battery using solution combustion synthesis: Higher temperature and longer syntheses improves performance,” *Journal of Alloys and Compounds,* vol. 861, p. 157972, 2021.

[21] A. Klein, P. Axmann, C. Yada and M. Wohlfahrt-Mehrens, “Improving the cycling stability of Li_2MnO_3 by surface treatment,” *Journal of Power Sources,* vol. 288, pp. 302-307, 2015.

[22] S. Chennakrishnan, V. Thangamuthu, A. Subramaniyam, V. Venkatachalam, M. Venugopal and R. Marudhan, “Synthesis and characterization of li2mno3 nanoparticles using sol-gel technique for lithium ion battery,” *Materials Science-Poland,* vol. 36(2), pp. 312-319, 2020.

[23] T. Matsunaga, H. Komatsu, K. Shimoda, T. Minato, M. Yonemura, T. Kamiyama, S. Kobayash, T. Kato, T. Hirayama, Y. Ikuhara, H. Arai, Y. Ukyo, Y. Uchimoto and Z. Ogumi, “Dependence of structural defects in li2mno3 on synthesis temperature,” *Chemistry of Materials,* vol. 28, pp. 4143-4150, 2016.

[24] M. Yoshio and H. Noguchi, “A review of positive electrode materials for lithium-ion batteries,” in *Lithium-Ion Batteries: Science and Technologies*, Japan, Springer Science+Business Media, 2009, pp. 9-46.

[25] S. Rajarathinam, S. Mitra and . R. . K. Petla, “Li_2MnO_3 rich-$LiMn_{0.33}Co_{0.33}Ni_{0.33}O_2$ integrated nano-composites as high energy density

lithium-ion battery cathode materials," *Alectrochimica Acta,* vol. 108, pp. 135-144, 2013.

[26] P. Guan, L. Zhou, Z. Yu, Y. Sun, Y. Liu, F. Wu, Y. Jiang and D. Chu, "Recent progress of surface coating on cathode materials for high-performance lithium-ion batteries," *Jornal of Energy Chemistry,* vol. 43, pp. 220-235, 2020.

[27] L.-P. Yang, X.-J. Lin, X. Zhang, W. Zhang, A.-M. Cao and L.-J. Wan, "General synthetic strategy for hollow hybrid microspheres through a progressive inward crystallization process," *Journal of the American Chemical Society,* vol. 138, pp. 5916-5922, 2016.

[28] C. Li, H. P. Zhang, L. J. Fu, Y. P. Wu, E. Rahm, R. Holze and H. Q. Wu, "Cathode materials modified by surface coating for lithium ion batteries," *Electrochimica Acta,* vol. 51, p. 3872–3883, 2006.

[29] G.-r. Hu, J.-c. Cao, Z.-d. Peng, Y.-b. Cao and K. Du, "Enhanced high-voltage properties of $LiCoO_2$ coated with $Li[Li_{0.2}Mn_{0.6}Ni_{0.2}]O_2$," *Electrochimica Acta,* vol. 149, pp. 49-55, 2014.

[30] W. Hua, B. Schwarz, R. Azmi, M. Muller, M. S. Darma, M. Knapp, A. Senyshyn, M. Heere, A. Missyul, L. Simonelli, J. R. Binder, S. Indris and H. Ehrenberg, "Lithium-ion (de)intercalation mechanism in core-shell layered $Li(Ni,Co,Mn)O_2$ cathode materials.," *Nano Energy,* vol. 78, p. 105231, 2020.

[31] L. Shen, H. Li, E. Uchaker, X. Zhang and G. Cao, "General strategy for designing core-shell nanostructured materials for high-power lithium ion batteries," *Nano Letters,* vol. 12, pp. 5673-5678, 2012.

[32] H. Chen, Y. Lu, H. Zhu, Y. Guo, R. Hu, R. Khatoon, L. Chen, Y.-J. Zeng, L. Jiao, J. Leng and J. Lu, "Crystalline SnO_2/amorphous TiO_2 core-shell nanostructures for high-performance lithium ion batteries," *Electrochemica Acta,* vol. 310, pp. 203-212, 2019.

[33] Y. K. Sun, S. T. Myung, B. C. Park, J. Prakash, I. Belharouak and K. Anime, "High energy cathode material for long life and safe lithium batteries," *Nature Material,* vol. 8, pp. 320-324, 2009.

[34] J. H. Ju and K. S. Ryu, “Synthesis and electrochemical performance of Li $(Ni_{0.8}Co_{0.15}Al_{0.05})_{0.8}(Ni_{0.5}Mn_{0.5})_{0.2}O_2$ with core–shell structure as cathode material for Li-ion batteries,” *Journal of Alloys and Compounds,* vol. 30, pp. 7985-7992, 2011.

[35] I. Bin-Mat-Arishad, B. Wimarshana and A. Fly, “Influence of voltage profile and fitting technique on the occuracy of lithium-ion battery degradation identification through the voltage profile model.,” *Journal of Energy Storage,* vol. 70, p. 107884, 2023.

[36] M. Doyle, T. F. Fuller and J. Newman, “Modeling of galvanostatic charge and discharge of the Lithium/Polymer/Insertion cell.,” *Journal of The Electrochemical Society,* vol. 140, pp. 1526-1533, 1993.

[37] I. Bin-Mat-Arishad, B. Wimarshana and A. Fly, “Influence of voltage profile and fitting technique on the occuracy of lithium-ion battery degradation identification through the voltage profile model.,” *Journal of Energy Storage,* vol. 70, p. 107884, 2023.

[38] W. Kohn and L. J. Sham, “Self consistent equations including exchange and correlation effects,” *Physical Review,* vol. 140, pp. 1133-1138, 1965.

[39] J. Slater and H. C. Verma, “The theory of complex spectra,” *Physics Review,* vol. 34, pp. 1293-1322, 1929.

[40] J. P. Perdew and W. Wang, “Generalized gradient approximation for the exchange correlation hole of many-electron system,” *Physics Review B,* vol. 45, pp. 13244-13249, 1991.

[41] J. C. Cuevas, “Introduction to density functional theory,” *Physics Review,* pp. 1-29, 1694.

[42] J. P. Perdew, K. Burke and Enzerhof, “Generalized gradient approximation sample,” *Physics Review,* vol. 118, pp. 3865-3868, 1996.

[43] E. Elatner, T. Frauenhem, E. Kaxiras, G. Seifert and S. Suhai, “Density functional tight binding of semi emperical methods in an Ab Initio era,” *Physics Review B,* vol. 3, pp. 7260-7268, 2000.

[44] M. Buhl, “DFT parameters for periodic tables,” *Journal of Chemistry,* vol. 9, pp. 4006-4017, 2013.

[45] C. Neto, F. N. Guinea, N. M. Peres, K. S. Novoselov and A. K. Gein, “Density functional tight binding,” *Physics Reviews,* vol. 1, pp. 63-66, 2009.

[46] T. Frauenheim, “Density functional theory based on tight binding methods,” *journal of physics,* vol. 8, pp. 9-13, 2016.

[47] Y. Kudoh and A. H. Taketa, “Local density approximation for the exchange correlation energy of an electronic system,” *Physical Chemical Mineral,* vol. 13, pp. 233-237, 1986.

[48] J. M. Haile, I. Johnston, A. J. Malinckrodt and S. Mckay, “Molecular dynamics simulation: elementry methods,” *Computers in Physics,* vol. 7, pp. 625-625, 1993.

[49] J. R. Perilla, B. C. Goh, C. K. Cassidy, B. Liu, R. C. Bernardi, T. Rudack, H. Yu, Z. Wu and K. Schulten, “Molecular dynamics simulations of large macromolecular complexes,” *Current Opinion in Structural Biology,* vol. 31, pp. 64-74, 2015.

[50] R. A. Burkingham, “The classical equation of state of gaseous hellium, neon, and argon,” *Proceedings of the Royal Society of London. Series A. Mathematics and Physical Science,* vol. 168, pp. 264-283, 1938.

[51] W. Smith and T. R. Forester, “A general-purpose parallel molecular dynamics simulation parkage,” *Journal of Molecular Graphics,* vol. 6, pp. 141-141, 1996.

[52] W. E. Wallace, “The born-mayer model for ionic solids and the hrats of formation and lattice spacings of alkali halide solid solutions,” *The Journal of Chemical Physics,* vol. 17, pp. 1095-1099, 1949.

[53] M. P. Tosi, “Cohesion of solids in the born model,” *Soild State Physics,* vol. 16, pp. 1-120, 1964.

[54] G. Gallavotti, “Statistical ensembles in statistical mechanics,” *Springer, Berlin, Heidelberg,* vol. 1, pp. 57-87, 1999.

[55] J. Glimm and A. Jaffe, “Classical statistical mechanics in quantum mechanics,” *Springer, New York, NY,* vol. 1, pp. 28-42, 1987.

[56] D. Brown and J. H. Clarke, “A comparison of constant energy, constant temperature and constant pressure ensembles in molecular dynamics simulations of atomic liquids,” *An International Journal at the Interface Between Chemistry and Physics ,* vol. 51, pp. 1243-1252, 1984.

[57] S. J. Clark and M. D. Segall, “First principle method using CASTEP,” *Z. Kristall,* vol. 220, pp. 567-570, 2005.

[58] Z. Ma, Z. Zheng, X. Tao, T. Hui, H. Yu and F. Bei, “Stabilization of Li_2MnO_3 phase by Mg doping suppressing irreversible oxygen loss and Mn ions migration,” *Journal of Alloys and Compounds,* vol. 977, p. 173367, 2024.

[59] L. Song, Z. Tang, Y. Chen, Z. Xiao, L. Li, H. Zheng, B. Li and Z. Liu, “Strcutural analysis of layered Li_2MnO_3-$LiMO_2$ (M=$Ni_{1/3}Mn_{1/3}Co_{1/3}$, $Ni_{1/2}Mn_{1/2}$) cathode materials by Rietveld refinement and first principle calculations,” *Ceramics International,* vol. 42, pp. 8537-8544, 2016.

[60] N. Yabuuchi, R. Hara, M. Kajiyama, K. Kubota, T. Ishigaki, A. Hoshikawa and S. Komaba, “New O2/P2-type Li-excess layered mnaganese oxides as promising multi-functional electrode for rechargeable Li/Na batteries,” *Advanced Energy Materials,* p. 1301453, 2014.

[61] W. Wen, S. Chen, Y. Fu, X. Wang and H. Shu, “A coreeshell structure spinel cathode material with a concentration-gradient shell for high performance lithium-ion batteries,” *Journal of Power Sources,* vol. 274, pp. 219-228, 2015.

[62] R. C. Longo, C. Liang, F. Kong and K. Cho, “Core-shell nanocomposites for improving the structural stability of Li-rich layered oxide cathode materials for Li-ion batteries,” *ACS Applied Materials and Interfaces,* vol. 10, pp. 19226-192234, 2018.

[63] J. A. Elliott, M. Benedict and M. Dutt, “Applications of DL POLY to modelling of mesoscopic particulate systems,” *Molecular Simulations,* vol. 00, pp. 1-9, 2006.

[64] G. W. Watson, E. T. Kelsey, N. H. de Leeuw, D. J. Harris and S. C. Parker, “Atomistic simulation of dislocations, surfaces and interfaces in MgO,” *Journal of the Chemical Society, Faraday Transactions,* vol. 92, p. 433, 1996.

[65] J. B. Goodenough and Y. Kim, “Challenges for rechargeable li batteries,” *Chemistry of Materials,* vol. 22, p. 587–603, 2010.

[66] T. Mogashoa, R. S. Ledwaba and P. E. Ngoepe, “Analysing the implications of charging on nanostructured Li_2MnO_3 cathode materials for lithium-ion battery performance,” *Materials,* vol. 15, p. 5687, 2020.

[67] Z. Zhang, S. Zhao, B. Wang and H. Yu, “Local redox reaction of high valence manganese in Li_2MnO_3-based lithium battery cathodes,” *Cell Reports Physical Science,* vol. 1, p. 100061, 2020.

[68] S.-J. Kim, M.-C. Kim, D.-H. Kwak, G.-H. Lee, H.-S. Choe and K.-W. Park, “Highly stable TiO_2 coated Li_2MnO_3 cathode material for lithium-ion batteries,” *Journal of Power Sources,* vol. 304, pp. 119-127, 2016.

[69] G. Jain, J. Yang, M. Balasubramanian and J. J. Xu, “Synthesis, electrochemistry, and structural studies of lithium intercalation of nanocrystalline Li_2MnO_3-like compound,” *Chemistry of Materials,* vol. 17, pp. 3850-3860, 2005.

[70] E. Jung, Y. Park, K. Park, M.-S. Kwon, M. Park, A. K. Sinha, B.-H. Lee, J. Kim, H. S. Lee, S. I. Chae, S. I. Cho, S.-P. Cho, K. T. Lee and T. Hyeon, “Synthesis of nanostructured P2-$Na_{2/3}MnO_2$ for high performance sodium-ion batteries,” *Chemical Communications,* vol. 55, pp. 4757-4760, 2019.

[71] H. Shang, Y. Zuo, F. Shen, J. Song, F. Ning, K. Zhang, L. He and D. Xia, “O2-type $Li_{0.78}[Li_{0.24}Mn_{0.76}]O_2$ nanowires for high-performance lithium-ion battery cathode,” *Nano Letters,* vol. 20, pp. 5779-5785, 2020.

[72] C. Jacob, J. Jian, Q. Su, S. Verkhoturov, R. Guillemette and H. Wang, “Electrochemical and structural effects of in situ Li_2O extraction from Li_2MnO_3 for Li-ion batteries,” *Applied Matreials and Interfaces,* vol. 7, pp. 2433-2438, 2015.

[73] M. D. Segall, P. J. Lindan and M. D. Probert, “First principle simulation ideas, illustration and the castep code,” *Physics Review B,* vol. 14, pp. 2717-2744, 2002.

[74] T. V. Mourik, M. Buhl and M. Gaigeot, “Density functional theory across chemistry, physics, and biology,” *Physics Review B,* vol. 8, pp. 20-23, 2014.

[75] G. R. Vignale, “DFT in magnetic fields,” *Physics Review Letter,* vol. 59, pp. 2360-2363, 1979.

[76] P. Hohenburg and W. Kohn, “Inhomogeneous electron gas,” *Physics Review B,* vol. 136, pp. 864-871, 1965.

[77] M. C. Payne, M. P. Tteer, D. C. Allan and T. A. Arias, “Iterative minimization techniques for ab initio total energy calculations: molecular dynamics and conjugate gradients,” *Review of Morden Physics,* vol. 64, pp. 1045-1097, 1992.

[78] T. R. Somo, T. E. Mabokela, D. M. Teffu, T. K. Sekgobela, B. Ramogayana, M. J. Hato and K. D. Modibane, “A comparative review of metal oxide surface coatings on three families of cathode materials for lithium ion batteries,” *Coatings,* vol. 11, pp. 744-765, 2021.

[79] H.-H. Sun, J.-Y. Hwang, C. S. Yoon, A. Heller and C. B. Mullins, “Capacity degradation mechanism and cycling stability enhancement of AlF_3-coated nanorod gradient $Na[Ni_{0.65}Co_{0.08}Mn_{0.27}]O_2$ cathode for sodium-ion batteries.,” *ACS Nano,* vol. 12, pp. 12912-12922, 2018.

APPENDIX A

CONFERENCE PRESENTATIONS

1. Makhubela P.G, Kgatwane K.M, Ledwaba R.S, and Ngoepe P.E, “Multi-Scale Modelling of P2 and O2-Type Materials for Utilization as Core-Shell Materials”, *South African Institute of Physics*, July 2022.
2. Makhubela P.G, Kgatwane K.M, Ledwaba R.S, and Ngoepe P.E, “Generating and Modeling the O2-$Li_{0.69}MnO_2$ and O3-Li_2MnO_3 Type Materials for Utilization as Core-Shell Materials”, *Center for High Computing Performance (CHPC)*, Nov 2022.
3. Makhubela P.G, Kgatwane K.M, Ledwaba R.S, and Ngoepe P.E, “Generating and Modelling the O2-$Li_{0.69}MnO_2$ and O3-Li_2MnO_3 Type Materials for Utilization as Core-Shell Materials” *Chem4Energy*, March 2023.
4. Makhubela P.G, Kgatwane K.M, Ledwaba R.S, and Ngoepe P.E, “Variation of Statistical Ensembles to Optimisse Complex Core-Shell Cathode Model: A Molecular Dynamics Approach”, *South African Institute of Physics*, July 2023.
5. Makhubela P.G, Kgatwane K.M, Ledwaba R.S, and Ngoepe P.E, Structural and Electronic Properties of Delithiated Li_2MnO_3 Material: A DFT Study, *Faculty of Science and Agriculture Research Day*, September 2023.
6. Makhubela P.G, Kgatwane K.M, Ledwaba R.S, and Ngoepe P.E, Structural and Electronic Properties of P2 and O2-Type Layered Lithium Manganese Oxides as Potential Coating Materials, *RAPDASA-RobMech-PRASA-AMI*, October 2023
7. Makhubela P.G, Kgatwane K.M, Ledwaba R.S, and Ngoepe P.E, Structural and Electronic Properties of Delithiated Li_2MnO_3 Material: A DFT Study, *Center for High Computing Performance (CHPC)*, December 2023

PUBLICATIONS

1. Makhubela P.G, Kgatwane K.M, Ledwaba R.S, and Ngoepe P.E, Structural and Electronic Properties of P2 and O2-Type Layered Lithium Manganese Oxides as Potential Coating Materials, *MATEC Web of Conferences: RAPDASA-RobMech-PRASA-AMI*, 2023